A 14.5 million-year record of East Antarctic Ice Sheet fluctuations from the central Transantarctic Mountains, constrained with cosmogenic ^{3}He, ^{10}Be, ^{21}Ne, and ^{26}Al

Allie Balter[1,2], Gordon Bromley[2,3], Greg Balco[4], Holly Thomas[1], Margaret S. Jackson[3]

[1]School of Earth and Climate Sciences, University of Maine, Orono, Maine, USA

[2]Climate Change Institute, University of Maine, Orono, Maine, USA

[3]Geography, National University of Ireland, Galway, Ireland

[4]Berkeley Geochronology Center, Berkeley, California, USA

Correspondence to: Allie Balter (abalter@ldeo.columbia.edu)

Abstract. The distribution of moraines in the Transantarctic Mountains affords direct constraint of past ice-marginal positions of the East Antarctic Ice Sheet (EAIS). Here, we describe glacial-geologic observations and cosmogenic-nuclide exposure ages from Roberts Massif, an ice-free area in the central Transantarctic Mountains. We measured cosmogenic ^{3}He, ^{10}Be, ^{21}Ne, and ^{26}Al in 168 dolerite and sandstone boulders collected from 24 distinct deposits. Our data show that a cold-based EAIS was present, in a configuration similar to today, for many periods over the last ~14.5 Myr, including the mid-Miocene, Late Pliocene, and early-to-mid Pleistocene. Moraine ages at Roberts Massif increase with distance from, and elevation above the modern ice margin, which is consistent with a persistent EAIS extent during glacial maxima, and slow, isostatic uplift of the massif itself in response to trough incision by outlet glaciers. We also employ the exceptionally high cosmogenic-nuclide concentrations in several boulders, along with multi-isotope measurements in sandstone boulders, to infer extremely low erosion rates (<< 5 cm/Myr) over the period covered by our record. Although our data are not a direct measure of ice volume, the Roberts Massif glacial record indicates that the EAIS was present and similar to its current configuration during at least some periods when global temperature was believed to be warmer and/or atmospheric CO_2 concentrations were likely higher than today.

1 Introduction

In this paper, we describe glacial deposits preserved in the central Transantarctic Mountains (TAM, Figure 1) that provide unambiguous evidence for the presence of the East Antarctic Ice Sheet (EAIS), in a configuration similar to today, for periods of the middle Miocene, late Pliocene, and early to middle Pleistocene. Our chronology therefore provides geologic targets for ice volume reconstructions derived from marine proxy records and sea-level estimates. Current estimates of pre-Pleistocene EAIS ice volume are based largely on δ^{18}O of benthic foraminifera (e.g., Shevenell et al., 2008), which primarily records global temperature and ice volume, and farfield sea-level indicators (e.g., Miller et al., 2005), such as raised shorelines (e.g., Rovere et al., 2014). These proxy records (e.g., Holbourn et al., 2013), along with stratigraphic evidence from ice proximal sediment cores (Levy et al., 2016) and modeling studies (Gasson et al., 2016), suggest that during the middle Miocene the EAIS oscillated between states both larger and

smaller than present in response to fluctuations in CO_2 and temperature. After ~14 Ma, such proxy records suggest general presence of the EAIS, but with potentially significant retreat during past warm periods, such as the mid-Pliocene Warm Period (3.3–3.0 Ma) (e.g., Dutton et al., 2015 and references therein), when temperatures are thought to have been 2–3°C warmer than preindustrial (Haywood et al., 2013) and CO_2 was ~400 ppm (Pagani et al., 2010; Seki et al., 2010). Although valuable for elucidating long-term trends in sea-level change, these proxy records do not directly record the volume of specific ice sheets. In contrast, glacial deposits from ice-free areas of Antarctica itself provide direct geologic evidence for past ice sheet variability.

Previous geomorphic and glacial chronologic studies in the Transantarctic Mountains (TAM), a ~3000 km-long topographic barrier through which outlet glaciers of the EAIS drain into the Ross Sea Embayment (Figure 1), suggest the presence of pre-Pleistocene glacial deposits. Two distinct categories of deposits characterize the Antarctic glacial-geologic record: basal tills of the Sirius Group (e.g., Mayewski, 1975; Mercer, 1972), which indicate at least one period of temperate glaciation, and thin, bouldery drifts and moraines deposited by ice frozen to the bed (e.g., Prentice et al., 1986), which overlie the older temperate deposits. In southern Victoria Land, Schaefer et al., (1999) reported a minimum age of > 10 Ma for Sirius Group tills at Mt. Fleming. Similarly, relict subglacial flood deposits in the Coombs Hills resulting from wet-based glaciation afford [3]He ages between ~8.5 and 10.5 Ma, assuming zero erosion, and as much as ~15 Ma if erosion rates of 0.03–0.06 m/Ma are applied (Margerison et al., 2005). In the same region, [40]Ar/[39]Ar ages on in situ ash layers interbedded with cold-based ablation tills in the Asgard Range date the transition from temperate to polar glaciation to between 15 and 13.6 Ma (Sugden and Denton, 2004). The preservation of such deposits over the last ~15 Ma has been invoked as evidence for persistent polar desert conditions, and by extension the presence of the EAIS, since that time (Denton et al., 1993).

Chronologic constraints on the overlying cold-based deposits come primarily from surface-exposure dating, which has been employed at several locations throughout the TAM, including southern Victoria Land (Brook et al., 1995, 1993; Brown et al., 1991; Bruno et al., 1997; Ivy-Ochs et al., 1995; Strasky et al., 2009); Beardmore (Ackert and Kurz, 2004) and Law (Kaplan et al., 2017) Glaciers in the central TAM; and Scott (Spector et al., 2017) and Reedy (Bromley et al., 2010; Todd et al., 2010) Glaciers in the southern TAM. Approximately 30 previously published exposure ages (see ICE-D:ANTARCTICA online database: http://antarctica.ice-d.org) indicate the preservation of cold-based glacial landforms in Antarctica that are at least 5 Ma in age. For example, a prominent boulder moraine in the Dominion Range, upper Beardmore Glacier, was dated with [3]He to 5.2 Ma (Ackert and Kurz, 2004). Similarly, [10]Be ages from erratic boulders at Reedy Glacier suggest deposition of the 'Reedy E drift' at > ~5 Ma (Bromley et al., 2010).
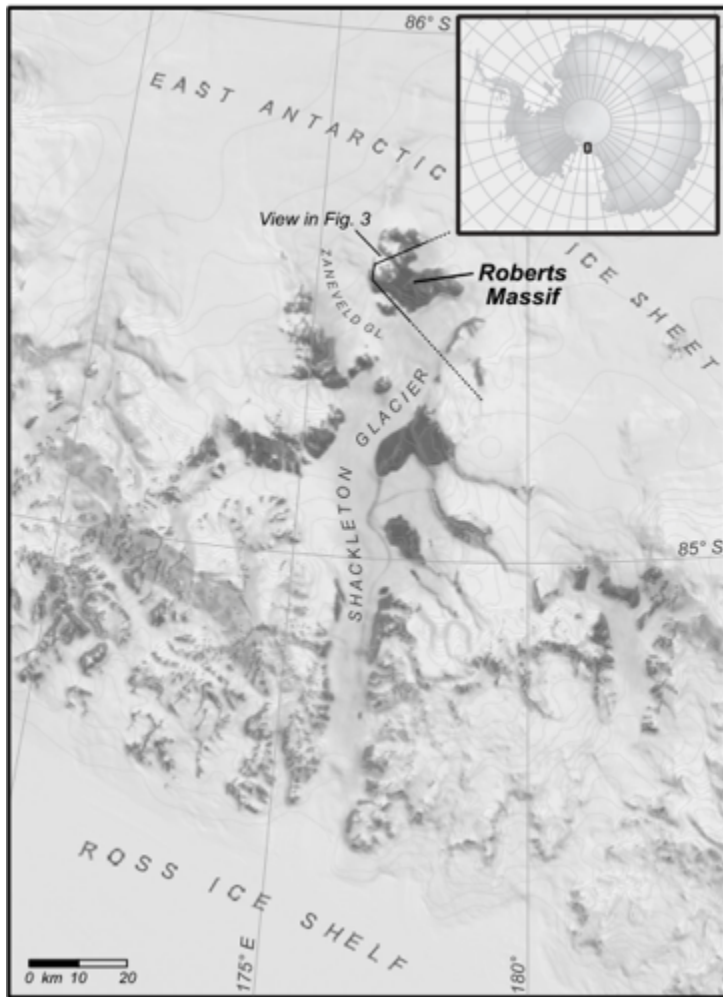
Figure 1. Location of Roberts Massif. The massif lies at the head of the Shackleton Glacier, which flows from the polar plateau of the East Antarctic Ice Sheet at ~2500 m elevation, down through the Transantarctic Mountains, to the Ross Ice Shelf near sea level. Base map generated from the MODIS MOA (Scambos et al., 2007) and Antarctic Digital Database via the Quantarctica compilation (http://quantarctica.npolar.no).

62   To further constrain the pre-Pleistocene configurations of the EAIS, we exploit the extensive moraine record at Roberts
63   Massif, a high-elevation site in the central TAM, where studies on nearby nunataks have suggested that old (> 5 Ma)
64   deposits exist (e.g., Ackert and Kurz, 2004). Roberts Massif (86.374°S, 177.135°W) is a ~100 km^2 ice-free area
65   situated at the head of Shackleton Glacier, an outlet of the EAIS (Figure 1). The massif is bounded to the south and
66   east by the EAIS, to the north and west by the upper Shackleton Glacier, and to the northeast by an unnamed branch
67   of Zaneveld Glacier. Today, the EAIS at Roberts Massif is cold based and the environment is that of a polar desert.
68   We employed cosmogenic ^{3}He, ^{21}Ne, ^{10}Be, and ^{26}Al to date moraines at Roberts Massif to create a comprehensive
69   glacial-geologic record for this site comprising 168 samples. Our record affords an unprecedented view of EAIS
70   variability in the central TAM over the last ~15 Ma and provides valuable new insight into EAIS behavior during
71   periods of the Miocene and Pliocene, when temperatures and atmospheric CO_2 were likely similar to or higher than
72   today.

2 Methods

2.1 Geomorphic Mapping and Sample Collection

Fieldwork took place during the 2015–2016 and 2016–2017 austral summers. In the field, we identified and mapped moraines, till deposits, and fault scarps on to 2 m-resolution satellite imagery provided by the Polar Geospatial Center, University of Minnesota. We collected samples for surface-exposure dating from the upper surfaces of erratic boulders located on moraine crests and drift sheets, focusing on boulders in stable positions (i.e., perched atop other boulders, not broken) and exhibiting minimal evidence for surficial erosion. Owing to the prevalence of nuclide inheritance documented by previous Antarctic cosmogenic studies (e.g., Stone et al., 2003; Todd et al., 2010), which is linked to incomplete erosion by cold-based ice of previously exposed surfaces, we sampled large (generally > 1 m tall), angular boulders, following the reasoning that such forms are (i) less likely to have been reworked from the underlying Sirius Group tills than visibly molded, striated, and/or polished cobbles of exotic lithologies, and (ii) more likely to have at least one side that is free of inherited nuclides.

We collected samples of ~1–5 cm thickness using either a hammer and chisel or drill and wedges. To characterize each sampled boulder fully and document its geomorphic context, we described, measured, sketched, and photographed each boulder from at least four different angles. We located samples in the field using an uncorrected handheld GPS unit (estimated horizontal precision typically ± 6 m), and measured elevations by barometric traverse from temporary benchmarks established using differentially corrected GPS and corrected to orthometric heights relative to the EGM96 geoid. The estimated vertical precision of the temporary benchmarks is between ± 0.05 and ± 0.3 m. For barometric differential elevation measurements relative to the benchmarks, we used a Kestrel 4000 barometric altimeter and looped between samples and benchmarks to correct for time-dependent changes in atmospheric pressure. The estimated total uncertainty in sample elevations measured using this procedure is ± 2.5 m, reflecting the precision of the DGPS surveys and the barometer, and the reproducibility of differential barometric elevation measurements of representative sites also surveyed by differential GPS in this and other studies. We measured topographic shielding at sample sites using handheld compass and inclinometer and the procedure described by Balco et al. (2008, with accompanying online material).

2.2 Cosmogenic-nuclide measurements

2.2.1 Cosmogenic helium-3 analyses

We measured cosmogenic ^{3}He concentrations in pyroxene separated from samples of Ferrar dolerite. To separate pyroxenes at the University of Maine Cosmogenic Isotope Laboratory, we followed a modified version of the method described by Bromley et al. (2014). We sieved crushed samples to isolate the 125–250 μm grain size fraction, which was boiled for two hours in 10% HNO_3 to remove Fe oxides and other weathering products. We then removed lighter minerals (mostly plagioclase) using a water-based heavy liquid with density 2.94 g/cm^3, and leached remaining material in 5% HF to dissolve adhering plagioclase and remove outer surfaces of pyroxene grains potentially enriched in implanted ^{4}He from U and Th decay (Blard and Farley, 2008; Bromley et al., 2014). Finally, etched pyroxenes were

passed through a magnetic separator and hand-picked to remove remaining contaminants under a binocular microscope.

We then measured ^{3}He concentrations in clean pyroxene separates at the Berkeley Geochronology Center using the BGC "Ohio" system, which consists of a MAP 215-50 sector field mass spectrometer with updated detectors and counting electronics, coupled to a fully automated gas extraction and purification system. Gas extraction on this system uses a laser "microfurnace" in which ~15-40 mg aliquots of pyroxene, encapsulated in Ta packets, are heated under vacuum using a 150W, 810 nm diode laser coupled to a coaxial optical pyrometer in a feedback loop allowing control of the pyrometer temperature. The pyrometer is calibrated by heating a thermocouple in an identical apparatus. However, note that precise temperature measurement is not necessary for this work. In most cases (Table S2), we extracted helium in an initial 15-minute heating step at 1225°C, followed by a second 15-minute heating step at 1325°C to ensure complete extraction. The second heating step typically contained 1–5% of total He released. We added additional heating steps for a few representative samples to test for complete extraction, and found He signals indistinguishable from blank. Gases released into the extraction line were purified by reaction with SAES getters and frozen to activated charcoal at 12 K, after which helium was released into the mass spectrometer at 33 K. In all cases, we measured ^{4}He signals on a Faraday cup and ^{3}He on a continuous dynode electron multiplier operated in pulse-counting mode.
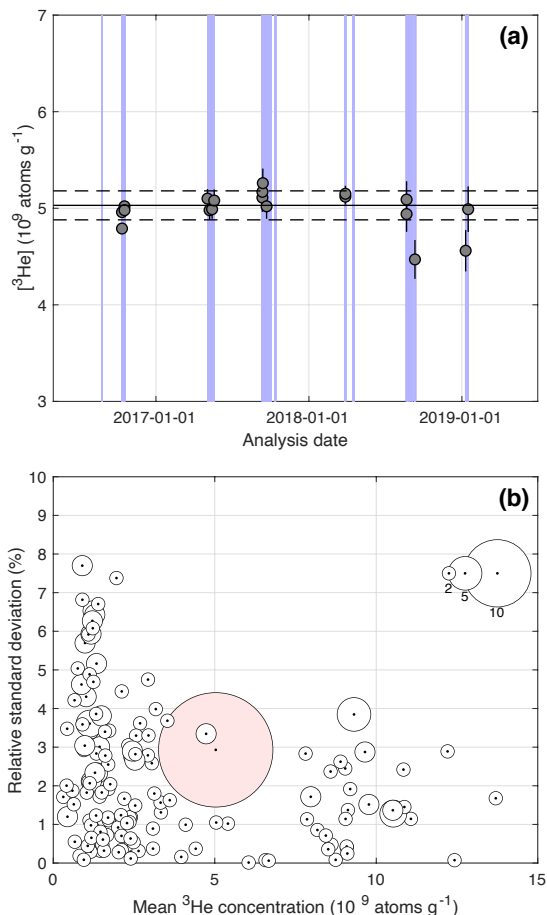
Figure 2. Quality-control data for ^{3}He measurements. a) Replicate analyses of CRONUS-P in all measurement periods during 2016-19. Blue lines indicate dates samples in this study were analyzed. Error bars show 68% confidence estimates (i.e., 1 sigma); relatively large uncertainties and poor reproducibility in final two measurement periods reflect unusually nonlinear helium sensitivity and relatively large scatter in analyses of gas standards during these periods. Horizontal lines show mean and standard deviation of all measurements. b) relative standard deviation of replicate analyses of 142 samples of Ferrar pyroxene analyzed during this study. 21 of these samples are not from Roberts Massif and therefore are not reported in this study but are included here for completeness. The size of the symbol indicates the number of times each sample was analyzed. The pink circle is CRONUS-P.

123   We quantified both ^{3}He and ^{4}He sensitivity by peak height comparison between samples and aliquots of custom-mixed

124   helium gas standards, calibrated using direct pressure measurements of both isotopes using Baratron capacitance

125   manometers, containing between 1.57×10^{-18} and 4.71×10^{-16} moles of ^{3}He and between 4.39×10^{-14} and 1.26×10^{-11}

126   moles of ^{4}He. Ferrar pyroxene has relatively high and highly variable ^{4}He concentrations, and the MAP 215 mass

127   spectrometer displays a significant pressure dependence on He sensitivity (Burnard and Farley, 2000), so accurately

128   quantifying machine sensitivity over a wide pressure range was an important aspect of this work. We addressed this

129   by (i) source tuning at He pressures similar to those expected for sample analyses to improve linearity in the pressure

130   range of interest, and (ii) ensuring that observed He pressures in sample analyses were bracketed within the pressure

131   range available from standard analyses. In many cases, this required discarding results of an initial analysis and

132   reanalyzing the sample with a different size aliquot calculated to match sample and standard pressures. Total process

133   blanks measured on empty Ta packets had less than 10^5 atoms ^{3}He and 10^{10} atoms ^{4}He, which is negligible for all

134   samples discussed here. Reported measurement uncertainties in ^{3}He concentrations include uncertainties from ^{3}He

135   counting statistics (typically 1–2%) as well as the variance in sensitivity inferred from gas standard analyses spanning

136   the pressure range of interest (typically 1–3%).

137   As additional quality control measures, we analyzed aliquots of the CRONUS-P pyroxene standard (Blard et al., 2015)

138   together with samples throughout each period of analysis, and made replicate analyses of a total of 121 pyroxene

139   samples as well as an additional 21 samples of Ferrar pyroxene from other Antarctic sites (Figure 2). In each of 6

140   distinct measurement periods between 2016-2019, we analyzed 2-4 aliquots of CRONUS-P. Although average

141   measured ^{3}He concentrations in individual measurement periods varied from $4.80 \pm 0.30 \times 10^9$ atoms/g to 5.14 ± 0.1

142    $\times 10^9$ atoms/g, data from different measurement periods were not distinguishable as separate populations. The mean

143   and standard deviation of 19 measurements during the entire period was $5.03 \pm 0.15 \times 10^9$ atoms/g (2.9%), which is

144   indistinguishable from the accepted value of 5.02×10^9 (Blard et al., 2015). Replicate analyses of other samples had

145   a mean relative standard deviation of 2.2% (Figure 2). As expected from counting statistics, replicate scatter varied

146   with ^{3}He concentrations, ranging from 3% for concentrations $< 2 \times 10^9$ atoms/g to 1.5% for concentrations $> 7 \times 10^9$

147   atoms/g.

148   Ferrar pyroxene is known to contain a non-zero concentration of non-cosmogenic (presumably magmatic) ^{3}He. Kaplan

149   et al. (2017), Margerison et al. (2005), and Ackert (2000) obtained maximum limiting concentrations for non-

150   cosmogenic ^{3}He of 5–7 $\times 10^6$ atoms/g, which are consistent with an unpublished estimate (Balco, unpublished data)

151   of $3.3 \pm 1.0 \times 10^6$ atoms/g. As this is 1.2% of the lowest total ^{3}He concentration measured in a Roberts Massif erratic

152   in this study, and 0.1 % of the average concentration observed, we disregard it and assume that all observed ^{3}He in

153   pyroxene is cosmogenic.

154   **2.2.2 Cosmogenic beryllium-10 and aluminum-26 analyses**

155   We purified quartz from sandstone samples using established physical and chemical procedures (e.g., Schaefer et al.,

156   2009) at the University of Maine Cosmogenic Isotope Laboratory. Chemical extraction of beryllium and aluminum

157   and preparation of BeO and Al_2O_3 targets took place at the University of Maine and Lawrence Livermore National

158   Laboratory (LLNL). Ratios of $^{10}Be/^9Be$ were measured relative to the 07KNSTD standard (Nishiizumi et al., 2007) at

159   LLNL and corrected for background ^{10}Be by procedural blanks with a range of 23,000–44,000 atoms. Al isotope ratios

160   are measured relative to the KNSTD standardization of (Nishiizumi, 2004), and corrected for a procedural blank of

161   75,000 ± 75,000 atoms. Note that blank corrections for both ^{10}Be and ^{26}Al are negligible for samples in this study.

162   One measurement of the CRONUS-A quartz standard (Jull et al., 2015) run together with these samples yielded 3.491

163   ± 0.047 x 10^7 atoms/g ^{10}Be and 1.494 ± 0.030 x 10^8 atoms/g ^{26}Al (Table S5), indistinguishable from accepted values

164   for both nuclides. Reported uncertainties for ^{10}Be and ^{26}Al measurements include uncertainties in AMS isotope ratio

165   measurement, process blanks, and $^9Be/^{27}Al$ concentrations.

2.2.3 Cosmogenic neon-21 analyses

167   We measured ^{21}Ne in the same quartz separates used for ^{10}Be analysis using the BGC "Ohio" noble gas mass

168   spectrometer system also used for ^3He measurements and described above. Aliquots of quartz samples were degassed

169   in two heating steps at 850° and 1100°C, and calculations of excess ^{21}Ne (see below) are based on total Ne released

170   in both heating steps. Ne isotope measurements at BGC use a ^{39}Ar spike to quantify and correct for the $^{40}Ar^{++}$

171   interference on mass 20, and are described in Balco and Shuster (2009). We quantified Ne abundances by peak height

172   comparison between samples and aliquots of an air standard containing between 5 x 10^{-16} and 2 x 10^{-14} mol Ne and

173   calibrated using a Baratron capacitance manometer. In contrast to helium, neon sensitivity was linear within this range

174   at all times. Corrections for mass discrimination, when necessary, are also based on the air standard and assumed

175   atmospheric $^{21}Ne/^{20}Ne$ and $^{22}Ne/^{20}Ne$ ratios of 0.002959 and 0.1020, respectively. A total of 20 analyses of the

176   CRONUS-A quartz standard during the period of this study yielded mean and standard deviation of 319.8 ± 6.3

177   Matoms/g (2% RSD) excess ^{21}Ne, indistinguishable from the accepted value of 320 Matoms/g (Vermeesch et al.,

178   2015).

179   Neon isotope ratios, as observed in previous studies for TAM sandstones, were indistinguishable from the

180   atmospheric-cosmogenic mixing line (see supplementary Table S3). However, Balco et al. (2019) and Middleton et

181   al. (2012) have also shown that significant concentrations of nucleogenic ^{21}Ne produced by decay of trace U and Th

182   are present in quartz from this lithology. To calculate cosmogenic ^{21}Ne concentrations in quartz samples, therefore,

183   we first calculated excess ^{21}Ne with respect to atmospheric composition, followed Balco et al. (2019) in assuming that

184   excess ^{21}Ne consists of both cosmogenic and nucleogenic ^{21}Ne, and estimated nucleogenic ^{21}Ne concentrations using

185   the following procedure. First, we measured excess ^{21}Ne concentrations in a set of six sandstone samples from ice-

186   proximal sites at upper Roberts Massif that have apparent ^{10}Be exposure ages less than 10 ka, and one additional

187   sample with an apparent ^{10}Be exposure age of 75 ka. Assuming that these samples have experienced a single period

188   of exposure, we calculated the ^{21}Ne concentration attributable to this exposure and subtracted it from total excess ^{21}Ne

189   concentrations to obtain estimates of nucleogenic ^{21}Ne; resulting mean and standard deviation for nucleogenic ^{21}Ne

190   estimates in these samples are 10.5 ± 2.8 Matoms/g, similar to but slightly higher than estimates for Beacon Group

191   sandstones in the Dry Valleys region (Balco et al., 2019; Middleton et al. 2012). We then measured U and Th

192   concentrations in quartz and computed apparent (U-Th)/^{21}Ne closure ages as described in Balco et al. (2019);

193   excluding one outlier attributed to a spurious Th measurement, the mean and standard deviation of apparent closure

194 ages is 603 ± 110 Ma. If we assume that all other sandstone erratics from Roberts Massif that we analyzed in this
195 study have a similar source and therefore a similar apparent closure age, we can estimate nucleogenic ^{21}Ne
196 concentrations using U and Th concentrations and this closure age estimate. Note that this apparent closure age is
197 older than the depositional age of the Beacon Group. If these sandstone samples are derived from the Beacon group,
198 therefore, it is most likely inaccurate as a cooling age. However, the provenance of the sandstone erratics is unknown,
199 and in any case this inaccuracy would not affect the assumption that Roberts Massif sandstone erratics have a single
200 characteristic apparent closure age. Table S4 shows the results of this procedure. For samples with less than 200
201 Matoms/g total excess ^{21}Ne, we measured U and Th concentrations in individual samples and applied the mean closure
202 age inferred from the ice-proximal samples, which resulted in subtraction of up to 20% of total excess ^{21}Ne as
203 nucleogenic and had a significant effect on results. For samples with higher ^{21}Ne concentrations, the uncertainty in
204 the nucleogenic ^{21}Ne estimate is negligible and we used an average value rather than measuring U and Th in individual
205 samples. For example, for samples from the Southwest Col on Misery Platform, discussed below, estimated
206 nucleogenic ^{21}Ne is less than 0.5% of total excess ^{21}Ne. Reported uncertainties for ^{21}Ne measurements, as for ^{3}He, are
207 derived from counting statistics as well as reproducibility of the gas standards.

208 **2.2.4 Treatment of replicates for cosmogenic noble gas measurements**

209 For the majority of samples, we made replicate ^{3}He and ^{21}Ne measurements and performed chi-squared tests on
210 replicate sets with the null hypothesis that all measurements on the same sample belong to a single population and
211 disagree only because of measurement uncertainty. If we could not reject the null hypothesis at 95% confidence, we
212 took the error-weighted mean of replicate analyses as the true nuclide concentration and the standard error as the
213 uncertainty. If the null hypothesis was rejected, we used the arithmetic mean and standard deviation. A caveat to this
214 procedure, however, is that we found that our ^{3}He results from CRONUS-P during the period of this study did not
215 pass a chi-squared test (p = 0.02), indicating that our internal uncertainty estimates for individual ^{3}He measurements
216 are underestimating the true scatter in multiple measurements of the same sample. Thus, we adjusted calculated
217 uncertainties upward when necessary such that no ^{3}He concentration has a relative uncertainty less than 2.9%, the
218 relative standard deviation of CRONUS-P measurements. ^{21}Ne results from CRONUS-A, on the other hand, passed
219 the chi-squared test (p = 0.35), so we did not make a similar adjustment to ^{21}Ne data. However, cosmogenic ^{21}Ne
220 concentrations do include an additional uncertainty derived from nucleogenic ^{21}Ne subtraction after averaging of
221 replicates.

222 **2.3 Surface exposure age calculations**

223 We calculated exposure ages from measured nuclide concentrations using Version 3 of the online exposure age
224 calculator described by Balco et al. (2008) and subsequently updated (http://hess.ess.washington.edu). We employed
225 the time-dependent "LSDn" scaling method of Lifton et al. (2014) and the Antarctic atmosphere model of Stone
226 (2000). Production rate calibration for ^{10}Be, ^{26}Al, and ^{3}He use the "primary" calibration data sets of Borchers et al.
227 (2016) for these nuclides, and we compute ^{21}Ne production rates by assuming a ^{21}Ne/^{10}Be production ratio of 4.03
228 (Balco et al., 2019; Balco and Shuster, 2009b; Kober et al., 2011). In contrast to exposure-dating studies that are

229   located at similar altitude and latitude to production rate calibration sites, our study involves significant extrapolations
230   from the locations of calibration data, mostly at low elevation and high latitude or high elevation and low latitude, to
231   the high-elevation-high-latitude sites at Roberts Massif. Scaling methods that can be fit equivalently to the calibration
232   data predict different production rates at our sites. Specifically, production rates predicted by LSDn scaling are ~15%
233   higher than those predicted by the scaling method of Lal (1991) and Stone (2000) (the 'St' and 'Lm' scaling methods
234   of Balco et al., 2008). However, at several high-elevation sites in Antarctica, including Roberts Massif, measured ^{10}Be
235   and ^{26}Al concentrations are significantly higher than values for production-decay saturation predicted by the St and
236   Lm methods, indicating that these methods overpredict production rates at high-elevation-high-latitude locations (see
237   discussion in https://cosmognosis.wordpress.com/2016/09/09/ saturated-surfaces-in-antarctica/). On the other hand,
238   saturation concentrations predicted by the LSDn method are consistent with the highest measured ^{10}Be and ^{26}Al
239   concentrations in Antarctica. Thus, we conclude that, at least in the high TAM, exposure ages calculated using LSDn
240   scaling are likely accurate, and exposure ages calculated using St/Lm scaling would be spuriously old.
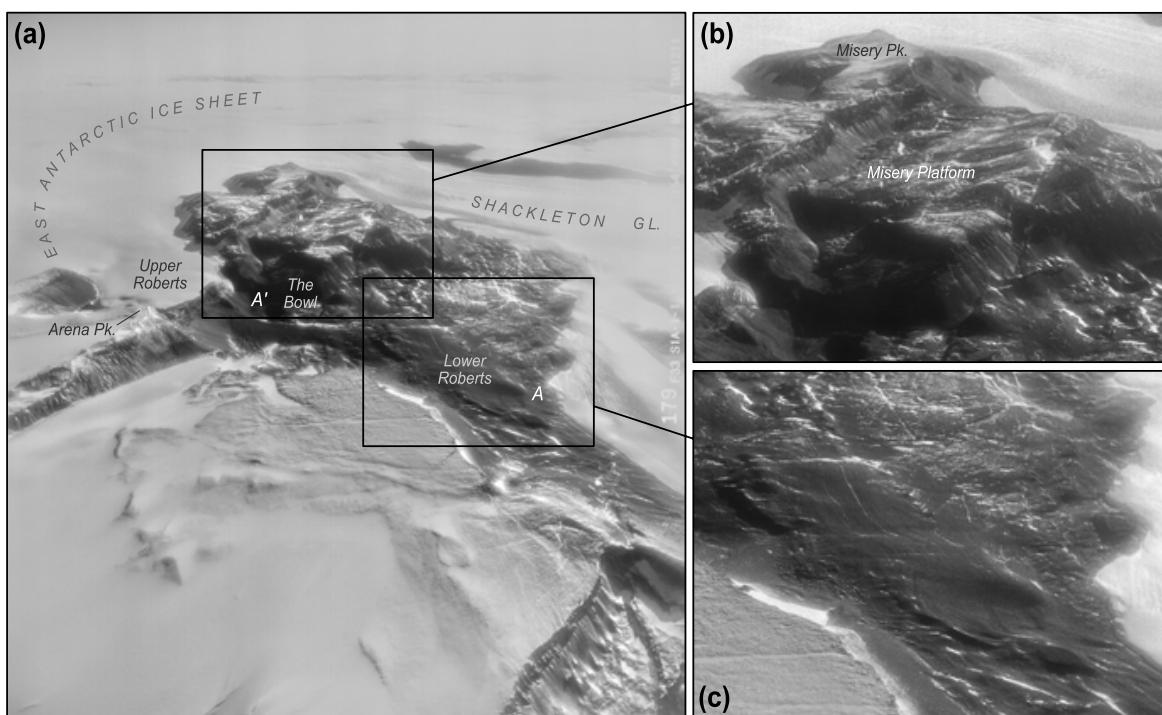
Figure 3. (a) Oblique aerial photograph of Roberts Massif looking west along the spine of the Transantarctic Mountains, with the East Antarctic Ice Sheet to the left. Enlargement (b) shows Misery Platform, which is the hanging wall of the large normal fault that bisects the massif. (c) shows the extensive moraine sequence at lower Roberts Massif. The moraine sequence at Upper Roberts (Fig. 7) faces west and is hidden from this viewing angle. The locations A and A' match Figure 4. Image is 1963 U.S. Navy trimetrogon aerial photograph, TMA 1211/179 R.

241   Additional uncertainties in exposure-age estimates derive from the choice of production rate calibration data.
242   Estimated total uncertainties for ^{10}Be exposure ages derived from calibration data are ~6% (Borchers et al., 2016).
243   Yet, any ^{10}Be calibration dataset that predicted significantly lower production rates, and therefore lower saturation
244   concentrations, would not be consistent with the ^{10}Be data from the Southwest Col (see discussion in section 4.3).
245   These data permit that we have underestimated ^{10}Be production rates, but not that we have overestimated them.

246 However, the majority of data in this study are ^{3}He exposure ages, and we have no similar constraint on ^{3}He production
247 rates. ^{3}He production rate calibration data display substantially more scatter than ^{10}Be, and estimates on total global
248 uncertainty for ^{3}He exposure dating range from less than 2% (Goehring et al., 2018) to more than 10% (Borchers et
249 al., 2016; Phillips et al., 2016). Production rate calibration uncertainty therefore may be significant for ^{3}He results.

3 Results

3.1 Field Observations

252 Roberts Massif is defined topographically by large-scale normal faulting that has produced escarpments as much as
253 ~1200 m in relief (Figure 3). These faults delineate a number of broad, sub-horizontal surfaces, including a lower-
254 elevation platform (hereafter 'Lower Roberts'), a middle-elevation platform, comprising the Misery Platform and
255 Upper Roberts sites, and the high peaks of the massif, including Misery Peak (2725 m) and Arena Peak (informal
256 name; 2700 m). Local bedrock comprises sandstones of the Beacon Supergroup and pyroxene-bearing Ferrar dolerite,
257 which includes a fine-grained variety and a friable, coarse-grained variety. Notably, the termini of the EAIS,
258 Shackleton Glacier, and the unnamed spur of Zaneveld Glacier at Roberts Massif are relatively free of debris,
259 containing only the occasional boulder. Further, we did not observe any evidence of glacial outwash or liquid water
260 at any of these margins, indicating that the ice bounding Roberts Massif is currently cold-based.

3.1.1 Lower Roberts

262 In the southern portion of the Lower Roberts area, a complex of faults forms a deep, back-tilted basin named "The
263 Bowl" by Hambrey et al. (2003). With the exception of a 100 m-relief bedrock hill, referred to here as the Central
264 Rise, and the Bowl, the Lower Roberts area exhibits relatively gentle topography (Figure 4). Dolerite bedrock surfaces
265 outcrop at several locations throughout Roberts Massif, and commonly exhibit glacial polish, striations, and molding
266 consistent with erosion beneath a wet-based glacier. Most of these bedrock outcrops are directly overlain by semi-
267 lithified, poorly sorted pockets of sediment (several meters thick in places), containing deeply striated gravel- to
268 cobble-sized clasts of heterogenous, non-native lithologies embedded in an olive-gray, clay-rich matrix (Figures 4 and
269 5). We interpret these sediments as lodgement tills associated with the Sirius Group. First described by Mercer (1972),
270 the Sirius Group occurs throughout the upper (> ~1500 m elevation) TAM as erosional remnants of clay-rich diamicton
271 that are correlated with at least one period of past temperate glaciation. An in-depth sedimentological study of glacially
272 eroded bedrock surfaces and Sirius Group tills at Roberts Massif, and other locations along upper Shackleton Glacier,
273 is provided by Hambrey et al. (2003).

274 Bedrock and Sirius Group tills are blanketed by patchy glacial drift, comprising primarily angular, cobble-to-boulder-
275 sized clasts with little-to-no fine-grained material (Figure 5). Ferrar dolerite is the most abundant lithology, although
276 this drift includes the occasional sandstone boulder, as well as rounded cobbles reworked from the underlying tills
277 described above. A key feature of this drift deposit is the abundance of open-work boulder moraines, which we
278 targeted for surface-exposure dating (Figure 6). These low relief (1–2 m high) ridges are composed primarily of large,
279 angular dolerite boulders and are oriented sub-parallel to the modern ice edge, marking former marginal positions of

the EAIS to the South and the unnamed spur of the Zaneveld glacier to the north. The sediments of these drifts and associated boulder-belt moraines exhibit characteristics typical of cold-based glaciation, being thin, patchy, and clast-supported with little-to-no fine-grained material (Figures 5 and 6) (Atkins, 2013). Furthermore, clasts are generally angular and lack the striations, polish, and molding associated with erosive wet-based ice.
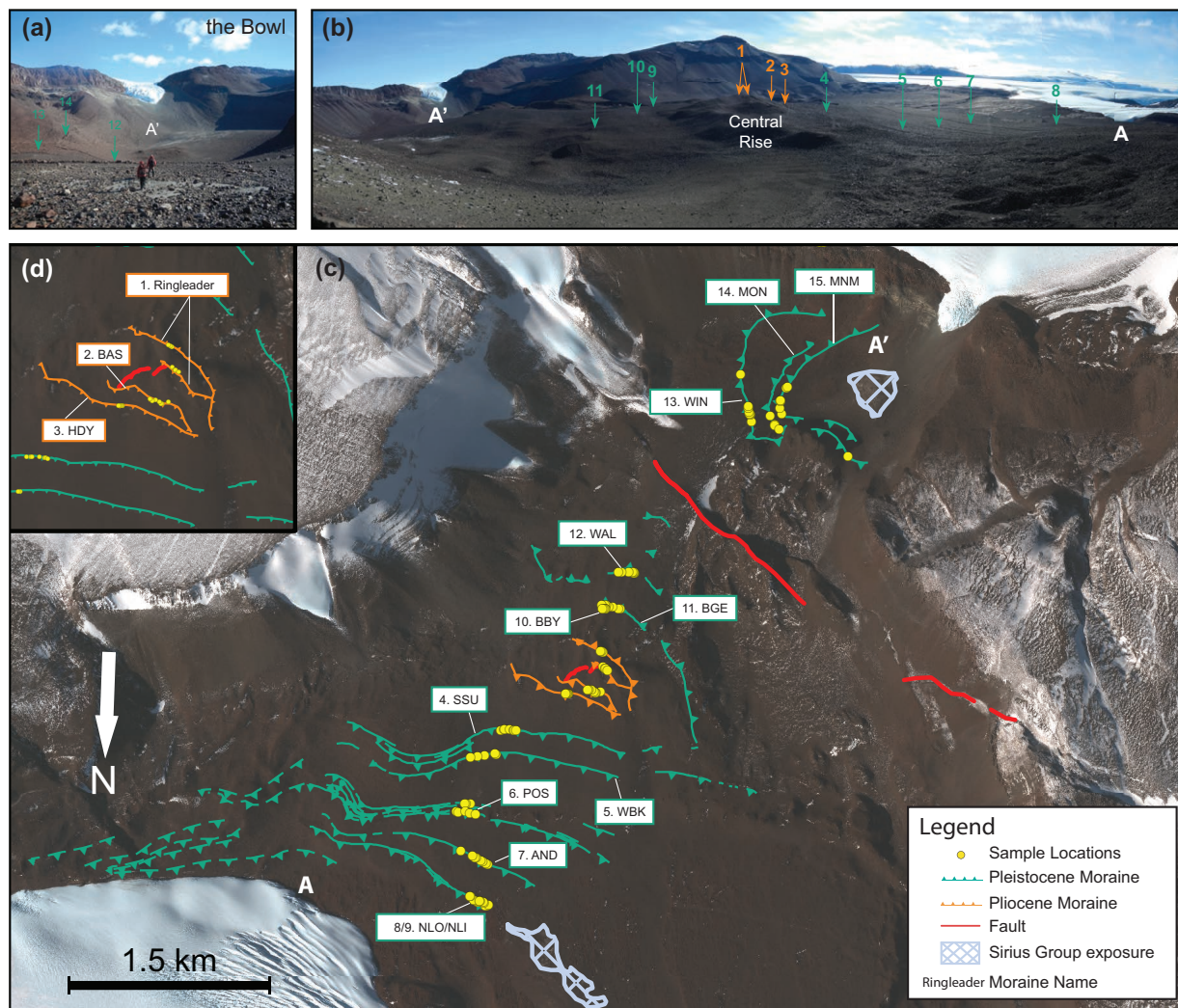
Figure 4: Map of Lower Roberts. a) Photograph of the Bowl, showing cold-based drift and moraines overlying Sirius Group deposits, which appear light gray, and b) photo of the Lower Roberts area. In (a) and (b), arrows point to sampled moraines, with numbers corresponding to moraine names in (c) and (d), and letters A and A' corresponding to positions in (c). c) Glacial geomorphic map showing moraines and sample locations at Lower Roberts, as well as the location of observed Sirius Group outcrops. The NLO/NLI and POS are moraine complexes that comprise two or more crests, and the BBY moraine is a short moraine segment just north of the BGE moraine. d) Closer view of the Pliocene-aged moraines encircling the Central Rise, shown in orange in (c). The base map is derived from Worldview-2 satellite imagery (copyright 2017, DigitalGlobe, Inc.).

We identified and sampled for surface-exposure dating 15 moraines throughout the Lower Roberts area. We focused on the most prominent, laterally continuous moraines, which comprise accumulations of stacked boulders, and avoided the numerous discontinuous moraine mounds and isolated erratic boulders, from which former ice marginal positions

287 are difficult to reconstruct. The stratigraphically oldest moraine in the Lower Roberts sequence, the Ringleader
288 moraine (informal name) encircles the summit of the Central Rise, indicating that north- and south-flowing ice masses
289 once converged to form a continuous ice surface across the Lower Roberts area at least ~170 m higher than the modern
290 ice margin to the north. From the Ringleader moraine, at the highest position in the Lower Roberts site, we sampled
291 northern (extending from Ringleader to A in Figure 4) and southern (extending from Ringleader to A' in Figure 4)
292 moraine transects. Listed in stratigraphic order, the northern transect included the BAS, HDY, SSU, WBK, POS,
293 AND, and NLO/NLI moraines (moraine initials correspond to informal names and sample ID suffixes listed in the
294 ICE-D Antarctica online database and Table S1); from the southern transect we sampled the BBY, BGE, WAL, WIN,
295 MON, and MNM moraines. Notably, the POS moraines constitute a complex of three main ridges, while the NLO/NLI
296 moraines comprise two distinct ridges spaced only by ~5 m.

297 The youngest deposit at Roberts Massif comprises a thin layer of sandstone and dolerite debris that extends several
298 tens of meters beyond the current ice margins. Clasts are relatively unweathered (i.e., exhibit minimal staining and/or
299 exfoliation), and exhibit fresh scuff marks [abrasions formed as cold-based ice drags entrained boulders across
300 underlying surfaces (Atkins et al., 2002)] (Figure 5f). With the exception of a few discontinuous segments, this unit
301 generally is not associated with distinct moraines. Based on strong similarities in position, morphology, and relative
302 weathering with deposits reported from other TAM sites (e.g., Todd et al., 2010), we correlate the youngest drift unit
303 at Roberts Massif with the most recent Late Quaternary expansion of Shackleton Glacier/EAIS and do not discuss it
304 further.

305 Outboard of this relatively unweathered limit, drift and moraine boulders become progressively more weathered with
306 distance from and elevation above the modern ice. For instance, dolerite boulders belonging to the outermost deposits
307 of the HDY, BAS, and Ringleader moraines (up to 3 km from and 170 m above the modern ice margin) exhibit dark
308 red staining, pitting of up to ~0.5 cm depth, exfoliation up to ~4 mm, and weathering rinds 1–2 mm thick, while the
309 presence of sandstone clasts is increasingly rare (Figure 6d). In contrast, dolerite boulders that we sampled on the
310 innermost moraines were generally blue-grey in color and lacked significant weathering characteristics, such as
311 staining or pitting (Figure 6c). Although the boulders on the outermost moraines at Roberts Massif display more
312 pronounced weathering than those on the inner moraines, the characteristics described here represent relatively
313 minimal surface weathering compared to slightly warmer and wetter Antarctic locations, such as the McMurdo Dry
314 Valleys. There, ~3 Ma clasts, which are similar in age to those on the HDY, BAS, and Ringleader moraines (Section
315 3.4), display pitting greater than 4 cm depth (Swanger et al., 2011). Additionally, we did not observe any cross-cutting
316 relationships between moraine crests throughout Lower Roberts, either on the ground or in satellite imagery.
317 Therefore, we conclude that moraines at this site increase in age with distance away from and elevation above the
318 modern ice sheet surface. Altogether, these surface-most deposits indicate that the Lower Roberts area records > 15
319 prior expansions of cold-based ice.

Figure 5: Views of drifts and tills described at Roberts Massif. a) The gray, fine-grained Sirius Group deposits atop striated dolerite bedrock; b) Sirius Group exposed in section in the Bowl, with 120 cm long pole for scale; c) Striated, glacially molded Sirius cobble embedded in a fine-grained matrix; d) Sample 16-ROB-089-COL, a freshly-scoured sandstone clast in the Bowl, likely deposited as a thin drift sheet atop older deposits during a Late Quaternary expansion of the EAIS; e) cold-based AND moraine, which is Pleistocene in age; and f) Misery B moraine, which is Miocene in age.

Figure 6: Photographs of moraines and sampled boulders at Roberts Massif. a) Blue-gray dolerite boulder 16-ROB-010-NLO on the second moraine from the modern EAIS in the Lower Roberts northern transect; b) Red-stained dolerite boulder 16-ROB-059-RIN on the Ringleader moraine, the outermost moraine in the Lower Roberts area; c) Relatively unweathered sandstone boulder 16-ROB-009-NLO; d) Red-stained/varnished sandstone boulder 16-ROB-062-RIN on the Ringleader moraine; e) Relatively unweathered, blue-gray dolerite boulder 15-ROB-064-MUS on the Musik moraine, the innermost moraine at Upper Roberts; and f) Weathered/red-stained dolerite boulder 15-ROB-038-ARM on the Arena moraine, the outermost moraine at Upper Roberts.

3.1.2 Upper Roberts

The Upper Roberts site is situated on a steep, west-facing slope of Arena Peak, directly adjacent to the northward flowing lobe of the EAIS that ultimately flows over the Bowl headwall (Figure 7). Here, we mapped glacial drift and moraines identical in character to those at Lower Roberts, indicating deposition by a cold-based EAIS. Similar to observations at Lower Roberts, a fresh-looking drift of sandstone and dolerite boulders extends several tens of meters beyond the modern ice edge. At the Upper Roberts site, that fresh deposit is associated with a low-relief (~1.5 m) ridge. We attribute this deposit to the most recent expansion of the EAIS during the Late Quaternary and do not discuss it further in this paper. We focused on five moraine ridges located along a vertical transect between ~60 m and 150 m above and oriented sub-parallel to the modern ice surface (2150 m). In order of descending elevation, we identified and sampled the Arena (2300 m), Eine (2260 m), Kleine (2240 m), Nacht (2220 m), and Musik (2220 m) moraines (informal names). Additionally, we mapped moraine segments preserved both within and above (up to ~2500 m elevation) this transect, but, owing to lateral discontinuity and poor preservation on high-gradient slopes, we did not sample these limits for surface-exposure dating. As at Lower Roberts, the general increase in boulder-surface weathering (Figure 6) and the absence of cross-cutting moraine stratigraphy (determined from field observations and satellite imagery; Figure 7) suggests that glacial deposits at Upper Roberts become older with increasing elevation above the modern EAIS.

3.1.3 Misery Platform

Misery Platform is a broad, gently sloping platform in the southwest part of Roberts Massif (Figures 3 and 8). Comprising the top surface of the hanging-wall block of a large normal fault, Misery Platform is bounded to the south by a ~300–340 m-high fault scarp. At the base of the scarp, we mapped a series of arcuate moraine ridges (here termed the Misery moraines), four of which we sampled for exposure-age dating (Figures 8 and 9). The southern edge of the footwall block, which includes Misery Peak (2723 m elevation), drops steeply to the EAIS surface at ~2200 m elevation, and exhibits south-facing, amphitheater-shaped valleys that are occupied partially by north-flowing lobes of the EAIS (Figure 8). The largest of these valleys is located directly south of the Misery Moraines, and its extension above the current surface of the EAIS suggests that this lobe of ice was significantly thicker in the past. Further, a thin drift of glacial erratics atop the footwall block at ~2550 m elevation mark where a north-flowing lobe of the EAIS overtopped the broad slopes east of Misery Peak and cascaded down the escarpment, where it deposited the Misery moraines on the platform below. This interpretation requires that the Misery moraines (a) postdate the formation of the fault scarp and (b) were deposited by an EAIS that was sufficiently thick (> 300 m above the current surface) to overtop the footwall block. Although the Misery moraines are similar in elevation to those sampled at Upper Roberts, they represent the highest former ice surface elevation of the EAIS examined in this study.
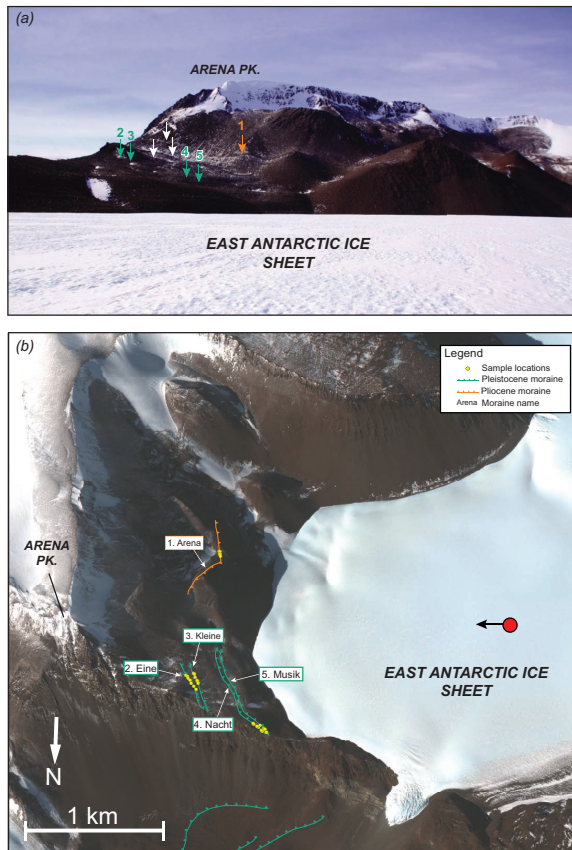
Figure 7. Upper Roberts Massif. a) Photograph of the Upper Roberts transect with moraines marked by arrows, numbered corresponding to sampled moraines in (b). White arrows in (a) denote undated moraines. b) Geomorphic map of Upper Roberts. The red circle and arrow shows the location and vantage of photo in (a). The base map in (b) is derived from Worldview-2 satellite imagery (copyright 2017, DigitalGlobe, Inc.).

351 Compared to moraines at Lower and Upper Roberts, the Misery moraines are relatively broad and high-relief (~2–5
352 m high) and comprise finer matrix material (silt-to-gravel). Moraine crests are mantled with angular dolerite boulders
353 exhibiting pronounced weathering features, including deep red-to-purple staining, 2–3 mm-thick weathering rinds,
354 and ventifaction pits of up to 2 cm depth. On the basis of these physical characteristics, they appear older than the
355 outermost moraines at both Lower and Upper Roberts. Therefore, we interpret the Misery moraines as cold-based ice-
356 marginal features marking the ostensibly oldest and most extensive EAIS terminus positions that we documented at
357 Roberts Massif. We used cross-cutting relationships of the Misery moraines to determine their stratigraphic order.
358 From outermost (oldest) to innermost (youngest), we sampled boulders on the following moraine crests: Misery D,
359 Misery A, Misery B, Misery C (note that the designations A-D are field designations reflecting the sequence of sample
360 collection, not the stratigraphic order; Figure 8). Importantly, we avoided sampling adjacent to overlapping moraine
361 segments.

362 Immediately outside of, and stratigraphically underlying, the Misery moraines, the weathered bedrock surface is
363 mantled with a thin patchy ablation till, dominated by dolerite boulders and a small number of sandstone clasts, and
364 associated with a coarse-grained sand and gravel deflation surface. We observed this unit throughout Misery Platform
365 and collected samples for surface-exposure dating from boulders on Southwest Col, located approximately 1.5 km
366 northwest of the Misery moraine complex and 400 m above the modern surface of Shackleton Glacier (Figure 8).
367 Here, the ablation till ('Southwest Col drift') mantles a bedrock surface of heavily stained and deeply exfoliated

coarse-grained dolerite. In places, granular sediments fill joints and depressions in the bedrock. These sediments are characterized by red-stained silt-to-gravel-sized grains, which may derive from the disintegration of the dolerite bedrock, and gravel-to-cobble-sized clasts of various lithologies. In contrast to the Sirius Group deposits observed elsewhere at Roberts Massif, boulders comprising Southwest Col drift are predominantly dolerite (as opposed to a broad mix) and generally more angular.

We sampled three dolerite clasts (1 boulder and 2 cobbles) and four sandstone clasts (3 boulders and 1 cobble), all of which are perched on bedrock and/or interstitial sediments, for surface-exposure dating. The surface of the dolerite boulder (15-ROB-28-COL) exhibits deep red staining and evidence of significant wind abrasion, except on the lee side where there is a thick red-brown weathering rind (Figure 9). The sandstone boulders (15-ROB-32-COL, 15-ROB-33-COL, and 15-ROB-34-COL) exhibit orange-to-red staining, surface varnish, and ventifaction of up to 4 cm depth. Based on the thin nature of this deposit, we interpret the Southwest Col drift as a cold-based ablation till deposited by the EAIS. Owing to its weathering state, we suggest that this deposit is the oldest glacial unit in our record. Surface-exposure ages from this site therefore provide a minimum-limiting age for temperate glaciation at Roberts Massif.

3.1.4 Summary of Field Observations

We mapped three primary surfaces at Roberts Massif (listed in stratigraphic order): glacially molded and striated dolerite bedrock, temperate-style tills belonging to the Sirius Group, and cold-based drifts associated with openwork boulder moraines. All samples collected for surface-exposure dating are derived from the cold-based deposits marking former positions of the EAIS. At both the Lower and Upper Roberts sites, weathering patterns and the lack of cross-cutting moraines suggest that relative moraine ages increase with distance from, and elevation above, the modern ice sheet margin. Deposits on Misery Platform (the Misery moraines and the Southwest Col drift) exhibit more advanced subaerial weathering than our other sites, indicating that these deposits are significantly older. In Section 4.2, we describe results from cosmogenic-nuclide measurements made on samples from 23 separate moraine ridges and one drift sheet.
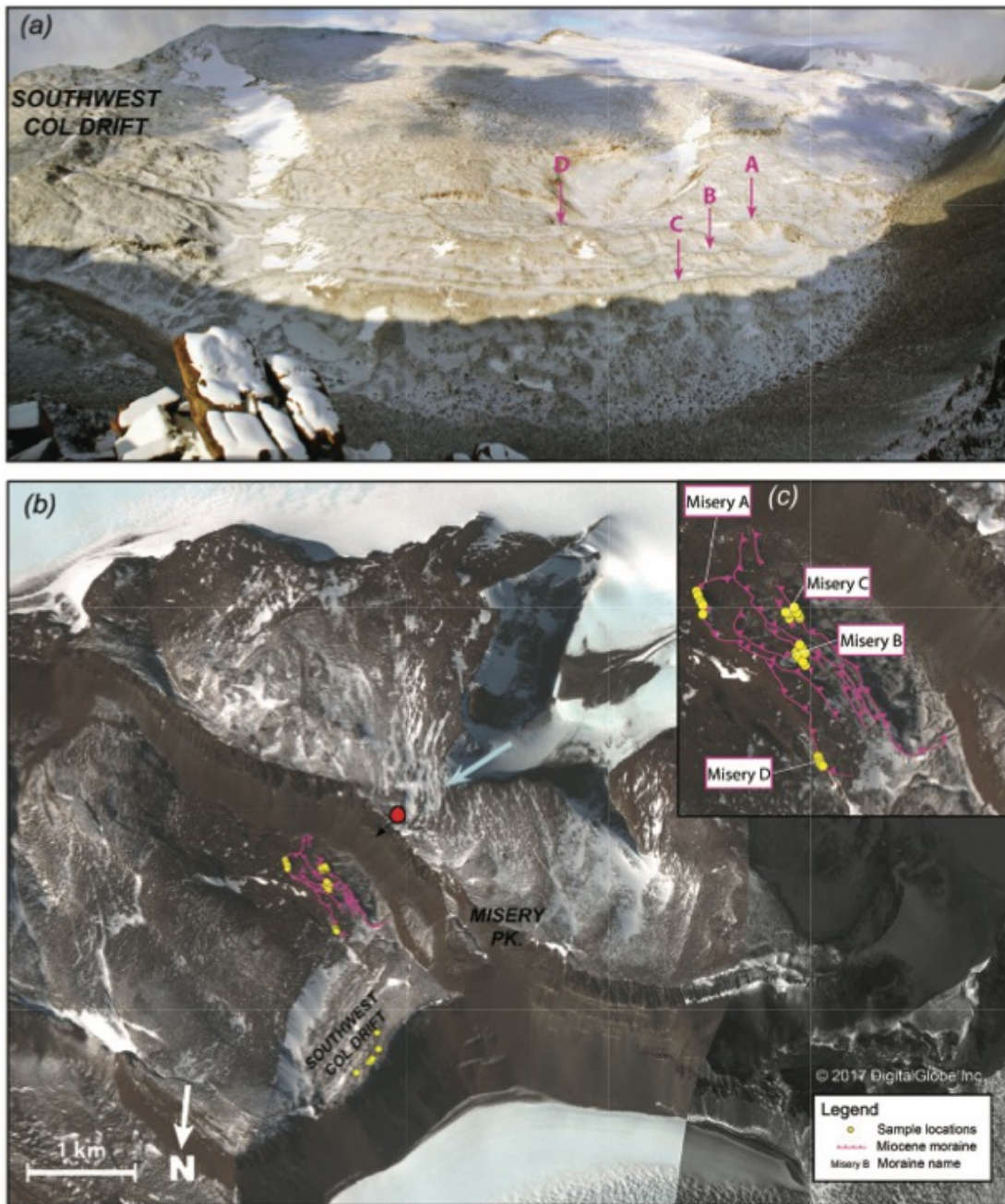
Figure 8: Map of Misery Platform. a) Photo of the Misery Moraines. Pink arrows point to the sampled Misery Moraines and are labelled with the corresponding moraine letter. The location of the Southwest Col Drift is also labeled. The photo was taken from the location of the red circle in (b) looking in the direction of the black arrow (vantage to the northeast). b) Geomorphic map of the Southwest Col area. The Southwest Col Drift mantles the bedrock outboard of the Misery moraines. The blue arrow denotes the direction of ice flow when the Misery Moraines were deposited. (c) Closer view of the Misery moraine complex. The base map in (b) and (c) is derived from Worldview-2 satellite imagery (copyright 2017, DigitalGlobe, Inc.).
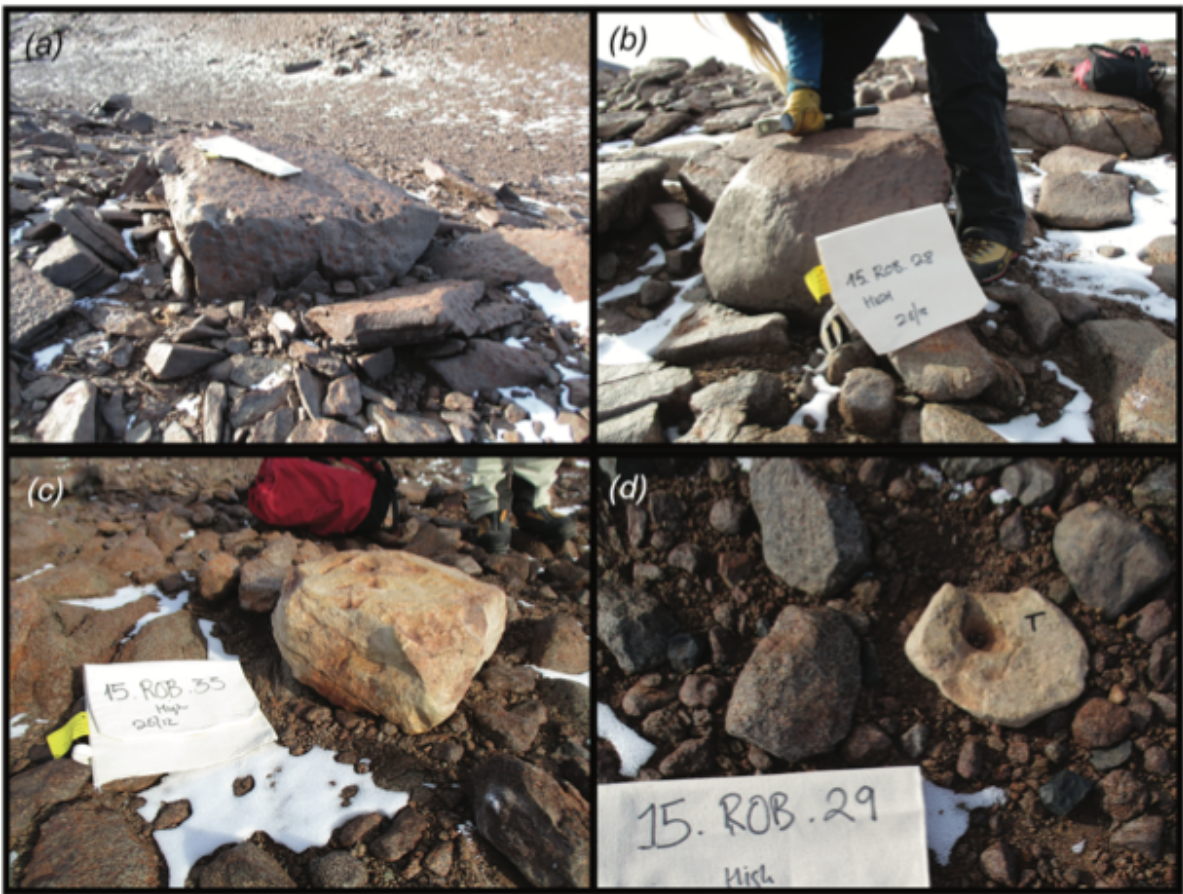
Figure 9: Photographs of boulders from the Misery Platform. a) Dolerite boulder 15-ROB-017-MZC on the Misery C moraine; b) Dolerite boulder 15-ROB-028-COL at the Southwest Col; c) Sandstone boulder 15-ROB-035-COL at the Southwest Col; d) Sandstone cobble 15-ROB-029-COL at the Southwest Col.

3.2 Results from Cosmogenic-Nuclide Measurements

We made 293 cosmogenic ^{3}He measurements in pyroxene from 155 dolerite boulders; 32 ^{21}Ne and 13 ^{10}Be measurements in quartz from 13 sandstone boulders; and two ^{26}Al measurements in quartz from two sandstone boulders (also measured for ^{21}Ne and ^{10}Be). Samples were derived from 23 distinct moraine crests and one glacial drift sheet (Southwest Col). Apparent exposure ages span two periods: ~13–8 Ma at Misery Platform and ~3 Ma–400 ka at Upper and Lower Roberts (Tables 1 and S1). "Apparent" exposure ages refer to the calculated age of the boulder given the measured nuclide inventory, assuming that the boulder has experienced only one period of exposure, with no erosion or burial during that time. Boulder information, nuclide concentrations, complete step-degassing results for ^{3}He and ^{21}Ne are summarized in Tables S2, S3, and S5, and the full dataset is archived online in the ICE-D:ANTARCTICA database (http://antarctica.ice-d.org). In this section, we summarize these cosmogenic-nuclide data

401 and highlight the possible effects of surface erosion and other geomorphic processes on exposure ages, which
402 ultimately lead us to estimates of the emplacement age of the moraines.

3.2.2 Constraints on erosion rates from paired ^{10}Be-^{21}Ne measurements

404 As the majority of landforms at Roberts Massif are several million years old, quantifying the magnitude of surface
405 erosion is key to accurate exposure-dating. Here, we summarize geochemical data and field observations that allow
406 us to place limits on long-term erosion rates. Four sandstone erratics at Southwest Col have ^{10}Be concentrations close
407 to predicted production-erosion saturation values, and apparent ^{21}Ne exposure ages of 9–12 Ma. As these samples
408 have nearly the highest concentrations of these nuclides yet measured on Earth, concentration measurements are
409 correspondingly (and unusually) precise, making it possible to use the paired ^{10}Be/^{21}Ne data to simultaneously infer
410 exposure ages and surface erosion rates from these samples (Figure 10) (Gillespie and Bierman, 1995; Lal, 1991).
411 Given the assumption that these samples have experienced continuous exposure at a steady erosion rate, the ^{10}Be/^{21}Ne
412 data imply true exposure ages in the range 12–15 Ma, but varying surface erosion rates in the range 0.5–3 cm/Myr.
413 These low erosion rates are consistent with our field observations pertaining to surface erosion of these sandstones as
414 described in Section 3.1.3.

415 Apparent ^{3}He exposure ages from three dolerite clasts also located on Southwest Col, and which therefore should have
416 the same true exposure age as the sandstone clasts, are 8.6 Ma, 10 Ma, and 11 Ma. Assuming that the true exposure
417 age of the deposit is no greater than 14.5 Ma, as implied by the two-nuclide data for the highest-nuclide-concentration
418 sandstone (15-ROB-032-COL) shown in Figure 10, this implies maximum erosion rates for the dolerite clasts of 3.8,
419 2.7, and 1.9 cm/Myr, respectively. Further assuming that the dolerite clast with the highest ^{3}He concentration (15-
420 ROB-028-COL) has been exposed at the drift surface for the longest period, and has therefore experienced mainly
421 surface weathering rather than exhumation from till, we propose that ~2 cm/Myr is likely a maximum limit on rock
422 surface erosion rates for dolerite surfaces in our study area. The assumption that this clast has been exposed at the
423 surface is supported by the fact that 15-ROB-028-COL is a boulder, while the rest of the dolerite surfaces we sampled
424 on Southwest Col are cobbles. If the deposit is younger than 14.5 Ma, an even lower erosion rate would be implied.
425 Although this is an extremely low surface weathering rate by global standards, it is nonetheless consistent with the
426 polar desert climate and the field observations described in section 3.1.3 (i.e., angular clasts with surface varnish and
427 minimal pitting).

3.2.3 Information about geomorphic processes from multiple-nuclide measurements

429 As on Southwest Col, we also measured multiple nuclides (^{10}Be and ^{21}Ne, and, in one case, ^{26}Al) in several sandstone
430 boulders on the Ringleader, WIN, MON, AND, and NLO moraines at Lower Roberts (Figure 11). Although sandstone
431 clasts are rare on these moraines, these data provide some insight into the exposure history of these boulders that we
432 can use to assess the importance of inheritance and post-depositional disturbance for moraine exposure ages.
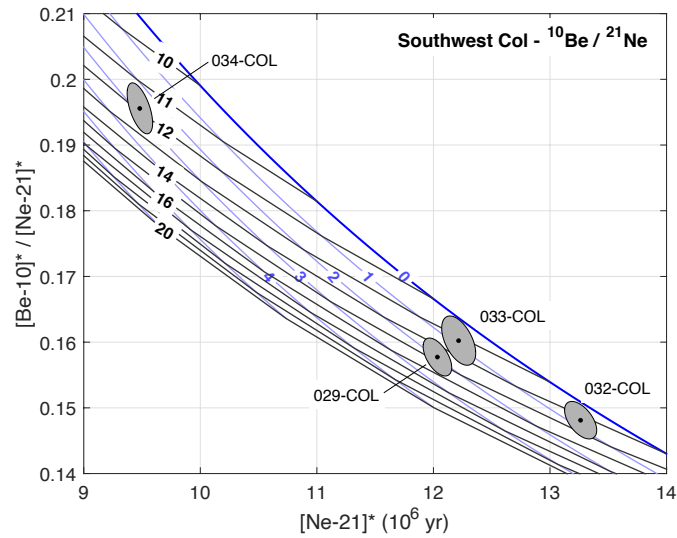
Figure 10. [10]Be-[21]Ne normalized two-nuclide diagram for Southwest Col sandstone erratics. Blue lines are isolines of constant steady erosion (cm/Myr); black lines are isolines of constant exposure age (Ma). The diagram is constructed using LSDn production rate scaling and a [21]Ne/[10]Be production ratio of 4.03 (Balco et al., 2019). Note that the x-coordinate, the [21]Ne concentration normalized to the production rate, is equivalent to the apparent [21]Ne exposure age. Although apparent [21]Ne exposure ages for these samples are 9.5–13 Ma, the two-nuclide diagram shows that the data are better explained by 12–15 Ma exposure at erosion rates between 0.5–3 cm/Myr.

433   In general, a boulder that has experienced a single period of exposure that is equal to the emplacement age of the

434   moraine should display concordant [10]Be, [21]Ne, and [26]Al ages that are the same as those of other boulders on the

435   moraine. For the Ringleader moraine (Figure 11), [10]Be-[21]Ne-[26]Al measurements are concordant at 2.8–3 Ma, therefore

436   consistent with simple exposure at negligible erosion, and lie in the center of the range of [3]He ages from dolerite clasts

437   on the same moraine (Figure 12). These observations suggest that (i) the sandstone boulders have experienced a single

438   period of exposure with minimal post-depositional exhumation or weathering, which is consistent with our field

439   observations as described in section 3.1.1, (ii) their exposure age most likely represents the true emplacement age of

440   the moraine, and (iii) two outliers in the [3]He age distribution can likely be attributed to both inheritance (one ~4 Ma

441   age) and post-depositional disturbance (one ~2 Ma age) .

442   In contrast, paired [10]Be-[21]Ne measurements on four boulders on the MON moraine and one on the WIN moraine

443   (Figure 11), both adjacent to the Bowl and emplaced by ice from upper Roberts overflowing the Bowl headwall (Figure

444   4), display discordant apparent ages. Additionally, apparent exposure ages from both sandstone and dolerite boulders

445   at these moraines are relatively scattered (coefficient of variance > 20%). The [10]Be-[21]Ne data (Figure 11) could be

446   explained either (i) by an extended period of steady erosion at an ice-free site prior to entrainment and deposition of

447   the clasts, or (ii) by repeated exposure and ice cover of the samples prior to emplacement. Both of these conditions

448   are likely if these boulders were sourced from the adjacent outcrop area of sandstone on the Bowl headwall (Figure

449   4a). Thus, we consider it most plausible that the apparent exposure ages of these sandstones reflect prior exposure

450   and, thus, overestimate the true age of the moraine. In general, these results imply that high scatter in exposure ages

451
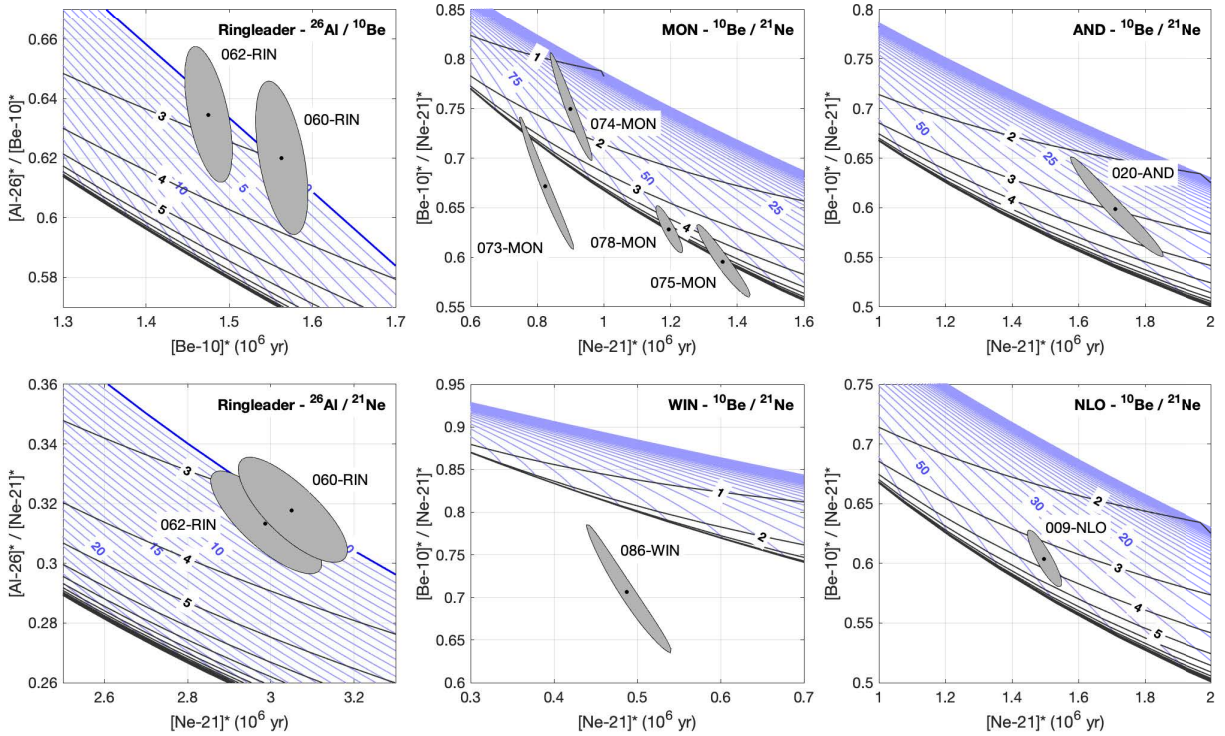
Figure 11. Two-nuclide diagrams for all sandstone erratics collected from lower Roberts Massif moraines. The construction of the diagrams is the same as in Fig. 10. Two-nuclide data for sandstones on the Ringleader moraine lie on the simple exposure line and are in agreement with [3]He ages, suggesting that these samples experienced a single period of exposure at negligible erosion, and their apparent ages are a good estimate of the true age of the moraine. On the other hand, paired nuclide data from sandstones on the MON, WIN, AND, and NLO moraines require either significant erosion or a multistage exposure history. An erosion explanation would predict that their apparent ages should be younger than [3]He ages on the same moraines; as this is not the case, these samples most likely experienced a multistage exposure history and therefore were emplaced with significant nuclide inheritance.

for moraines in the Bowl are most likely explained by inherited nuclide concentrations in clasts sourced from the adjacent headwall, and the true ages of the moraines are therefore likely close to the young end of their age distributions.

Finally, paired ^{10}Be-^{21}Ne measurements from the AND and NLO moraines (Figure 11), both at the ice-proximal end of the northern Lower Roberts transect, fall within the "erosion island" on the two-nuclide diagram, indicating that their true exposure ages are older than the apparent ages for either nuclide. In addition, these clasts have apparent ages higher than most ^{3}He ages from these moraines (Figure 12). Again, this is best explained if the scatter exhibited by these moraines is largely the result of inheritance.

Overall, although we have a relatively small number of multiple-nuclide data from sandstone boulders, our results demonstrate that (i) inheritance is unequivocally present in some moraine boulders and (ii) inheritance is likely most significant at moraines where boulders are likely sourced from a combination of far-traveled EAIS subglacial debris

471   and cliff fall within the massif itself. These scenarios are also consistent with the observation that boulders on moraines

472   at upper Roberts, which can only be derived from beneath the EAIS, exhibit substantially less scatter than moraines

473   at lower Roberts (Table 1 and Figure 12), where additional input from rockfall is likely. Overall, while none of our

474   observations exclude post-depositional disturbance as a potential source of scatter, they do show that inheritance is

475   likely a more important contributor. However, the small number of young outliers in our dataset (Figure 12) may

476   reflect the ablation of an ice core from the moraine.

477   **3.3 Outlier Elimination**

478   For each moraine dated, we measured cosmogenic nuclides in 6–8 individual clasts. We observed a variety of

479   distributions ranging from tightly grouped age sets, which likely reflect dispersion due to measurement uncertainties

480   alone, to highly scattered distributions with both old (indicative of nuclide inheritance) and young outliers (e.g., due

481   to ablation of an ice core from the moraine, subaerial weathering and/or post-depositional disturbance, such as rock

482   toppling or cracking). To interpret these age distributions and arrive at realistic estimates of the moraine age, we

483   utilized constraints from field observations, the stratigraphic ordering of the moraines, exposure-age trends across

484   moraine transects, and measurements of multiple nuclides in various clasts (see above).

485   We first considered geomorphic stratigraphy, weathering characteristics, and trends in exposure-age distributions to

486   identify and eliminate outliers. For Misery Platform, we utilized the cross-cutting relationships of the Misery moraines,

487   which elucidate relative age, to identify exposure ages that are outliers. Although we did not observe such cross-

488   cutting relationships at Upper and Lower Roberts, we exploited the fact that both apparent exposure ages and physical

489   weathering state increase with distance from and elevation above the modern ice margins to determine relative ages

490   of the moraines, and thus to identify likely outliers.

491   We performed an initial screening to remove outliers by assuming that the true depositional age of each moraine lies

492   within the range of measured exposure ages on this moraine. If true, then any exposure ages on one moraine that are

493   older than all exposure ages on a stratigraphically older moraine must be erroneous. Likewise, any exposure ages that

494   are younger than all ages on a stratigraphically younger moraine must also be erroneous. Applying this rule recursively

495   to stratigraphically ordered sets of moraines resulted in the rejection of 46 measurements on 22 boulders (Figures 12

496   and 13; Table S1). We also rejected 9 measurements on 5 boulders as outliers likely resulting from geomorphic

497   processes (i.e., inheritance or post-depositional disturbance), which were not rejected as stratigraphic outliers yet are

498   > 2σ beyond the main age population on that moraine (see Table S1). After this stratigraphic screening was complete,

499   we also rejected as outliers 14 non-concordant ^{10}Be and ^{21}Ne measurements on 10 sandstone boulders located on the

500   NOLO, AND, WIN, and MON moraines, as those boulders likely contain inherited nuclides (see discussion in Section

501   3.2.3). In total, we rejected 69 measurements on 37 boulders (Figures 12 and 13; Table S1).

502   The resulting boulder age distributions for each moraine exhibit a variety of forms. Many moraines (e.g., Arena, BAS,

503   Misery B moraines; Figures 12 and 13) display a central cluster approximating a normal distribution, and for these

504   moraines we assign the mean and standard deviation of the ages as the best estimate of the depositional age of the

505   moraine. Other moraines (e.g., SSU, WAL, BGE) showed heavily skewed, bimodal, or scattered age distributions; for

506 these we provide age ranges rather than means in the discussion that follows. In the case of those high-scatter moraines,

507 it is likely that the true moraine age is closer to the younger end of the age range, as we identified inheritance as a

508 more likely contributor to moraine scatter than post-depositional disturbance (Section 3.2.3).

509 **3.4 Moraine ages**

510 In this section, we summarize moraine age estimates assuming zero surface erosion (Table 1; Figures 12 and 13); we

511 discuss the effects of this assumption in later sections.

512 **Lower Roberts:** The oldest dated moraine in the Lower Roberts area – Ringleader –dates to 2.94 ± 0.24 Ma. Along

513 a northward transect from the summit of the Central Rise to the modern ice margin, subsequent moraines yielded the

514 following ages (moraine initials correspond to informal names and sample ID suffixes listed in the ICE-D Antarctica

515 online database; Figure 12): BAS (2.94 ± 0.14 Ma), HDY (2.84 ± 0.08 Ma), WBK (1.62–2.84 Ma), SSU (1.90–2.95

516 Ma), POS (1.16–2.05 Ma), AND (1.08–1.63 Ma), NLO (1.07–1.58 Ma), NLI (0.54–2.09 Ma). A similar transect

517 extending southward from the Central Rise provides the following moraine ages: BBY (1.55–2.69 Ma), BGE (1.41–

518 2.93 Ma), WAL (1.50–2.80 Ma), WIN (0.51–1.00 Ma), MON (0.54 ± 0.01 Ma), and MNM (0.40–0.87 Ma). As

519 discussed in section 3.2.3, this southern transect displays the highest degree of age scatter, potentially due to the

520 incorporation of rockfall from the surrounding escarpments.

521 **Upper Roberts:** Moraine ages at Upper Roberts display a high degree of internal consistency and are reported here

522 from highest moraine to lowest: Arena (2.64 ± 0.13 Ma); Eine (1.19 ± 0.14 Ma); Kleine (1.18 ± 0.16 Ma); Nacht (1.11

523 ± 0.10); and Musik (0.61–1.10 Ma) (Figure 12). As noted in section 4.1, undated moraine segments located above the

524 Arena moraine represent higher surface levels of the EAIS, potentially prior to ~2.6 Ma. Additionally, undated

525 moraine segments situated between the Arena and Eine moraines, which differ in elevation by ~45 m, may account

526 for the temporal gap between these two limits.

527 **Misery Moraines:** Approximately 1.5 km southeast of the Southwest Col drift (~14.5 Ma, section 3.2.2), the Misery

528 moraines yielded ages (listed from outermost moraine to innermost) of 7.94 ± 0.23 Ma (Misery D; n = 4), 7.93 ± 0.23

529 Ma (Misery A; n = 1), 7.99 ± 0.06 Ma (Misery B; n = 8), and 7.63 ± 0.29 Ma (Misery C; n = 5) (Figure 13). We

530 consider a young population of ages, between ~4 and 6 Ma, on the Misery A and Misery C moraines to be outliers as

531 the bulk of ages from the complex cluster around 8 Ma. Due to the excellent internal consistency of these age

532 populations, we consider it unlikely that the 8 Ma population reflects inheritance, as that mechanism typically

533 introduces considerable scatter to the data set (Balco, 2011).
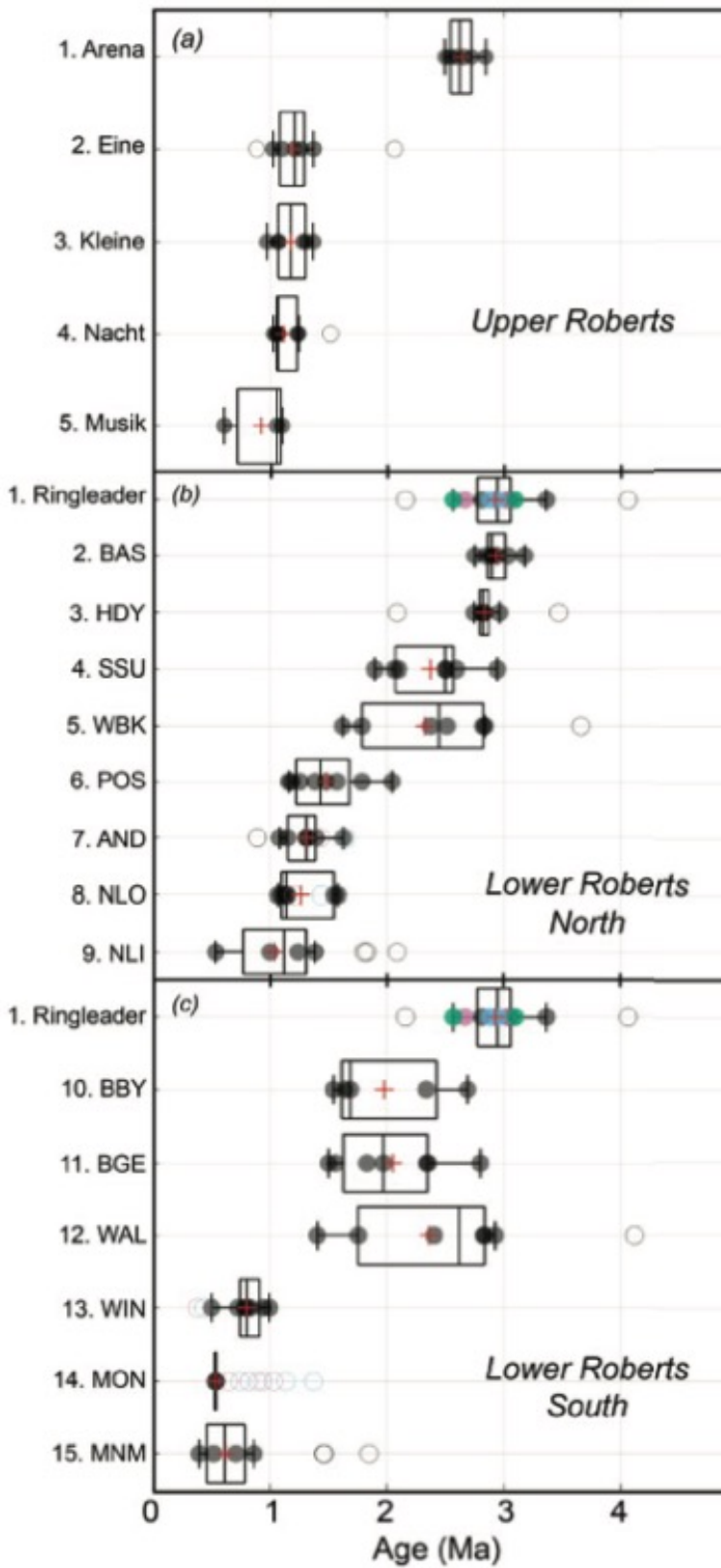
Figure 12: Boxplots showing moraine ages for the Plio-Pleistocene part of the Roberts Massif record. Moraines for each site (Upper Roberts and Lower Roberts northern and southern transects) are listed in stratigraphic order, with the outermost moraine at the top of each panel. Moraine numbers in (a) correspond to those in Figure 7, while moraine numbers in (b) and (c) correspond to those in Figure 4. The Ringleader moraine is shown in both panels (b) and (c), as it is the uppermost moraine in both Lower Roberts transects. [3]He ages are black, [21]Ne ages are blue, [10]Be ages are pink, and [26]Al ages are green. Outliers are shown as open circles. The average moraine age is denoted by a red plus symbol.
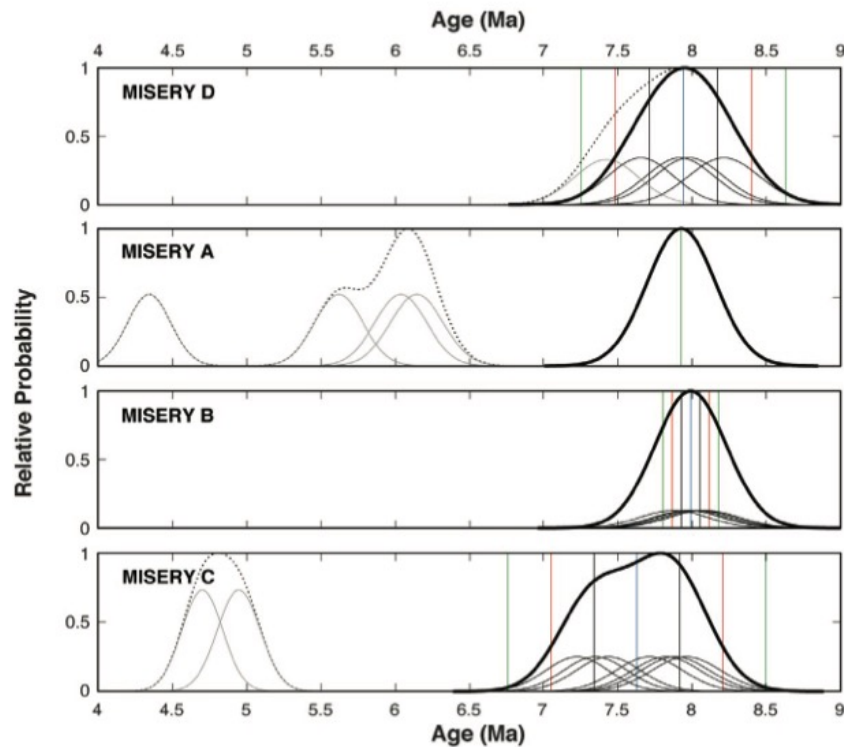
Figure 13: Camel plots (i.e., normal kernel density functions) for the four Misery moraines. The arithmetic mean of the reduced dataset is denoted by the blue line, while the 1σ, 2σ, and 3σ uncertainty envelopes are shown in black, red, and green, respectively. Dotted black lines show the summed probability distributions for the full dataset, including outliers shown in gray, while the thick black lines show the probability distribution for the reduced dataset.

4 Discussion

Cosmogenic-exposure ages on moraines and glacial drift at Roberts Massif afford unprecedented insight into Late Cenozoic variability of the EAIS. The record begins at ~14.5 Ma (Southwest Col drift), while distinct ice-marginal positions date to ~8 Ma and between ~3–1 Ma. As described in Section 3.1, all moraines are characteristic of cold-based glacial conditions and are oriented sub-parallel to the modern EAIS margins, suggesting ice configuration similar to today at high elevation in the central TAM. Recognizing the influence of Ross Sea ice on even the uppermost reaches of transverse EAIS outlet glaciers (Mercer, 1968; Bockheim et al., 1989; Denton et al., 1989; Orombelli et al., 1990; Denton and Hall, 2000; Bromley et al., 2010, 2012), we speculate that the Roberts Massif moraines formed when Ross Sea ice (either an ice shelf or grounded ice sheet) buttressed Shackleton Glacier and thus that ice configuration in the Ross Sea Embayment was similar to today for considerable parts of our record. In the following sections, we discuss the length of the Roberts Massif glacial-geologic record and address the climatic implications of our findings.

4.1 Uplift at Roberts Massif

Relative to previous glacial-geologic archives from Antarctica, the Roberts Massif record is exceptionally long (~14.5 Ma). At all three sites described in section 3.1, moraine age increases with distance from and elevation above the modern EAIS, with the oldest site (Misery Platform) ostensibly indicating the thickest ice. One hypothesis to explain the age-elevation relationship at Roberts Massif is that, while the massif itself has remained isostatically stable for duration of our record, the surface elevation of the EAIS during glacial maxima has lowered systematically over time. Alternatively, the configuration of the EAIS during glacial maxima has remained roughly constant for the duration of the record, but the underlying bedrock has undergone uplift due to tectonism, dynamic topography, and/or isostasy, processes relevant to the millions-of-years timescale. Tectonic uplift at Roberts Massif since ~15 Ma likely was minimal; apatite fission thermochronology in the central TAM suggests that major faulting due to tectonism was complete by ~30 Ma (Fitzgerald, 1994; Miller et al., 2010). However, over the last 3 Myr, approximately 40 m of uplift at Roberts Massif may be attributed to dynamic topography (Austermann et al., 2015), though this value cannot account fully for the ~3 Ma ice positions situated ~170 m (Ringleader moraines) and ~180 m (Arena moraine) higher than the modern EAIS at Lower and Upper Roberts, respectively.

Instead, isostatic rebound resulting from deepening of outlet glacier troughs (i.e., removal of rock and replacement by less dense ice) may account for much of the apparent moraine elevation loss through the Roberts Massif record. While large portions of EAIS outlet glaciers, including Shackleton Glacier, are likely frozen to the bed, and thus minimally erosive, regions of these glaciers are thick enough to be at the pressure melting point today (Golledge et al., 2014), and thus eroding their beds (Bader et al., 2016; Graly et al., 2018). Removal of several hundred meters of rock since the mid-Miocene would therefore result in isostatic rebound of a few hundred meters (Van der Wateren et al., 1999; Stern and Tenbrink, 1989). Although we cannot quantify total trough erosion over the course of our record, this magnitude of uplift is consistent with the observed elevational offset between relict moraines and the modern EAIS.

As well as elucidating deposition age, near-saturation concentrations of ^{10}Be on Southwest Col (15-ROB-033-COL) and ^{26}Al the Ringleader moraine (16-ROB-062-RIN) afford maximum-limiting values for isostatic uplift at Roberts Massif, both since ~14.5 Ma and during the last 3 Myr. For these samples, ^{10}Be and ^{26}Al concentrations become saturated (with respect to LSDn scaling) with erosion rates of ~2.3 g cm^{-2} Myr^{-1} and ~7 g cm^{-2} Myr^{-1}, respectively. If we assume that this apparent erosion rate reflects not removal of mass by surface weathering, but rather a decrease in atmospheric depth due to uplift, these erosion rate values provide maximum uplift rates. The ^{10}Be saturation erosion rate for 15-ROB-033-COL yields an uplift rate of ~24 m Myr^{-1} over the last ~14 Myr, indicating that the total maximum uplift over the course of the record is ~350 m, or ~70 m over the last 3 Myr. This estimate accounts for less than half of the elevation difference between the ~3 Ma Ringleader moraine and the EAIS margin (~170 m). In contrast, the ^{26}Al saturation erosion rate for 16-ROB-062-RIN affords a higher uplift rate of ~70 m Myr^{-1} over the last 3 Myr, or ~210 m over the Plio-Pleistocene portion of the record, a value that accounts for the full ~170 m elevation difference between the Ringleader moraine and the modern EAIS. Importantly, both the 24 m Myr^{-1} and 70 m Myr^{-1} values each represent maximum uplift rates under the assumption of zero erosion, meaning that the average pace of uplift during the Plio-Pleistocene may not have differed from that during the last ~14.5 Ma. In fact, because ^{26}Al does

582   not quite reach saturation in 3 Myr, it is likely that the 70 m Myr^{-1} is an overestimate. Moreover, the true uplift rate at

583   Roberts Massif probably was lower than those calculated here, since our field observations indicated that some, albeit

584   minor, post-depositional surficial erosion has taken place (Section 3.1).

585   Uplift of < ~200 m over the Plio-Pleistocene is consistent with cosmogenic-nuclide concentrations from the McMurdo

586   Dry Valleys, which indicate minimal vertical change during this period (Brook et al., 1995). Similarly, $^{40}Ar/^{39}Ar$ ages

587   on subaerial volcanic cones limit uplift to 300 m in the Dry Valleys over the past 3 Ma (Wilch et al., 1993) and < 67

588   m in the Royal Society Range over the past 7.8 Ma (Sugden et al., 1999). In contrast, Stern et al. (2005) posit that > 1

589   km of isostatic uplift throughout the central TAM has occurred since 35 Ma due to glacial erosion. If true, the

590   cosmogenic-nuclide concentrations presented here imply that nearly all of this uplift must have taken place between

591   35 and 14 Ma.

592   Given the likelihood of isostatic uplift over the long duration of our record, which potentially accounts for much of

593   the offset between moraine elevations and the modern EAIS, we cannot evaluate changes in ice thickness throughout

594   this ~14 Myr record with certainty. However, we emphasize that a large, cold-based ice sheet with configuration

595   similar to today was present during the dated parts of this record.

596   **4.2 Miocene presence of the EAIS**

597   The oldest dated glacial unit at Roberts Massif, Southwest Col drift, was deposited ~14.5 Ma and demonstrates that

598   the EAIS in the central TAM was cold based by at least the mid-Miocene (Figure 14). This finding aligns closely with

599   earlier work from the northern TAM that placed the transition to polar conditions at ~14–15 Ma (Denton and Sugden,

600   2005). We note that deposition of Southwest Col drift also coincided broadly with a mid-Miocene climatic shift

601   documented in the Olympus Range, McMurdo Dry Valleys, where well-preserved terrestrial and lacustrine fossils

602   interbedded with ash fall deposits have been interpreted as reflecting an 8°C cooling of Antarctic summers at ~14.5

603   Ma (Lewis et al., 2008). In addition, the age of Southwest Col drift, which provides a minimum-limiting age for cold-

604   based glaciation in the central TAM, is approximately coeval with the Mid-Miocene Cooling Transition (~15–13 Ma),

605   marked by a decline in global sea-surface and bottom-water temperatures (Lear et al., 2015) and atmospheric CO_2

606   concentrations (Zhang et al., 2013). Finally, Southwest Col drift affords minimum-limiting age constraint for the

607   underlying Sirius Group till at Roberts Massif and supports previously published surface-exposure data suggesting

608   that these temperate deposits are > 5 Ma (Ivy-Ochs et al., 1995; Schaefer et al., 1999).

609   Overlying Southwest Col drift, the ~8 Ma Misery moraines represent the oldest ice-marginal landforms identified at

610   Roberts Massif and suggest the presence of a large, cold-based ice sheet at that time. This EAIS configuration is

611   broadly coincident with elevated sea-surface temperatures (Herbert et al., 2016) and Antarctic Bottom Water

612   temperatures (Lear et al., 2015), and potentially higher atmospheric CO_2 (Sosdian et al., 2018) relative to the Plio-

613   Pleistocene. Therefore, our record suggests that a substantial EAIS occupied the central TAM at ~8 Ma despite

614   generally warmer-than-present climatic conditions (Figure 14).

4.3 Plio-Pleistocene presence of the EAIS

The majority of moraines in the Roberts Massif record date to ~3–1 Ma, thus documenting the persistence of a large EAIS during the Plio-Pleistocene transition and early Pleistocene (Figure 14). Because the uncertainties in our moraine ages (~0.1–0.5 Ma) exceed the 40-kyr climate cycles dominant during the pre-MPT world, we do not assign moraines to individual climate events, such as Marine Isotope Stages (i.e., Lisiecki and Raymo, 2005; Railsback et al., 2015). Nonetheless, moraines dated to > ~2.5 Ma indicate a large EAIS in the central TAM during times when global temperatures and atmospheric CO_2 were likely higher than today (Willeit et al., 2019).

Several moraines at Roberts Massif date to ~3 Ma (Ringleader, ~3 Ma; BAS, ~3 Ma; HDY, ~2.8 Ma; Arena, ~2.6 Ma), inviting the question of whether any of these landforms correspond to the Mid-Pliocene Warm Period (MPWP: ~3.3–3.0 Ma), which has garnered attention as a plausible analog for modern anthropogenic warming. The ongoing debate regarding the resilience of the EAIS during the MPWP bears two leading hypotheses: (i) that the EAIS was of similar extent, or potentially larger, than today during the MPWP (e.g., Sugden et al., 1993; Winnick and Caves, 2015) due to increased East Antarctic precipitation under warmer atmospheric conditions (Huybrechts, 1993); and (ii) that the EAIS was significantly smaller than today (Scherer et al., 2016; Webb et al., 1984) as a result of enhanced melting along marine margins (Pollard and DeConto, 2016) and associated structural collapse (Pollard et al., 2015). At Roberts Massif, moraines dating to the MPWP would support the first hypothesis; however, an absence of MPWP moraines neither proves nor disproves the second hypothesis, as geologic evidence for even a slightly smaller EAIS would lie beneath the modern ice sheet surface (Balco, 2015). Below, we address the possibility that any Roberts Massif moraines date to the MPWP, given the uncertainties associated with exposure dating (i.e., erosion, production rate error, and uplift).

First, we address the possibility that erosion of boulder surfaces, which acts to remove a portion of the cosmogenic nuclide inventory, yielded erroneously young apparent exposure ages for the Late Pliocene moraines. As shown in Section 3.2.3, concordant ^{10}Be-^{21}Ne-^{26}Al measurements on Ringleader sandstones afford an exposure age of ~3 Ma, consistent with the ^{3}He ages on that moraine, and both sandstone and dolerite boulders appear to have experienced relatively minimal erosion (i.e., angular, minimal pitting and exfoliation; Section 3.1.1). Applying the maximum surface erosion rate for dolerites of 2 cm/Myr, determined using the ^{3}He concentration of 15-ROB-028-COL (Section 3.2.2), the average dolerite age on Ringleader is 3.18 Ma and thus within the uncertainty of the apparent moraine age. Together, our field observations and cosmogenic-nuclide measurements suggest that the apparent age of the Ringleader moraine is not erroneously young due to surface erosion. As discussed in Section 4.1, the maximum possible error in moraine age due to uplift is the same as that for erosion, meaning that the inclusion of uplift has no significant impact on moraine age.

Next, we explore the potential effect of cosmogenic nuclide production-rate uncertainty on moraine age. The ^{10}Be production rate is accompanied by ~6% error and ^{3}He by ~10% error (Borchers et al., 2016), meaning that the Ringleader moraine could be ~6 % older (with a lower production rate) or younger (with a higher production rate), using the more precise ^{10}Be production rate as a limit (note: ^{10}Be and ^{3}He ages are statistically indistinguishable). However, we can use the boulder with the highest ^{10}Be concentration on Southwest Col (15-ROB-033-COL), which

651   is close to saturation, to provide a lower limit for the [10]Be production rate. Applying a production rate ~2% lower than
652   the globally calibrated production rate of Borchers et al. (2016), which we used to calculate the [10]Be ages presented
653   here, sample 15-ROB-033-COL becomes oversaturated with respect to LSDn scaling, suggesting that, at most, the
654   Ringleader moraine (the oldest in the Plio-Pleistocene sequence) is no older than ~3 Ma. Conversely, if the true
655   production rate is higher than that of Borchers et al. (2016), it is possible that the Ringleader moraine is up to 6%
656   younger (~2.8 Ma) than reported here. As there are no sandstones on the oldest landform in the Upper Roberts
657   sequence – Arena Moraine (~2.7 Ma) – we assess the full 10% range in [3]He production rate. Assuming a 10% reduction
658   in production rate, the Arena moraine could date to ~3 Ma, or the end of the MPWP.

659   In summary, we did not date any moraines unequivocally to the MPWP, suggesting that the EAIS was not significantly
660   larger than today during that time. However, given the dataset presented here, we cannot evaluate further the
661   configuration of the EAIS during the MPWP because evidence for the ice sheet extent during that time lies beneath
662   the modern glacier. Moreover, we note that our moraine chronology lacks landforms dating to the earlier Pliocene (~5
663   Ma), when conditions are thought to have been as warm as during the MPWP (Burke et al., 2018). Nevertheless, our
664   current dataset provides evidence for a large, cold-based EAIS in the central TAM during the Late Pliocene,
665   immediately following the MPWP, and in the early-to-mid Pleistocene.

666   **5 Conclusions**

667   Surficial deposits characteristic of cold-based glaciation at Roberts Massif span the Last Glacial Maximum to Mid-
668   Miocene, thereby providing an exceptionally long geologic record of glaciation for the central TAM. The preservation
669   of numerous, vertically offset ice-marginal deposits is most plausibly explained by the persistence of an EAIS similar
670   in configuration to today during multiple glacial maxima, accompanied by gradual isostatic uplift of Roberts Massif.
671   Coupled with extremely low erosion rates (<< 5 cm/Myr), the prevalence of cold-based deposition over the last ~14.5
672   Ma supports persistent polar desert climate conditions in East Antarctica since the mid-Miocene. Our record also
673   provides minimum-limiting age control for the underlying Sirius Group deposits, suggesting that at least some of the
674   temperate glacial deposits preserved in the TAM are older than 14.5 Ma.

675   Although the Roberts Massif record is not a direct measure of East Antarctic ice volume, our dataset indicates that the
676   EAIS was not any larger during the late Pliocene-early Pleistocene than it was during parts of the Miocene, even
677   though temperatures cooled progressively through the Plio-Pleistocene. Nonetheless, the absence at Roberts Massif
678   of ice-marginal deposits dating unequivocally to the MPWP highlights a critical area for continued investigation, since
679   distal paleoclimate evidence and model simulations suggest the EAIS was smaller than present at that time. Accepting
680   that geologic evidence for even a slightly smaller EAIS during the MPWP would lie beneath the modern ice sheet, we
681   cannot further evaluate the extent to which the EAIS was smaller during the MPWP with the current data set from
682   Roberts Massif.

683   In summary, the Roberts Massif dataset provides a long-term, terrestrial perspective of ice sheet extent in the central
684   TAM, and shows that the EAIS has been a persistent feature of this region since the mid-Miocene. Throughout this

685   record, the EAIS has maintained a configuration similar to today, which requires the presence of buttressing ice in the

686   Ross Sea Embayment, and by extension, West Antarctica, even during periods when global temperature and

687   atmospheric CO_2 concentrations likely were similar to or higher than present.
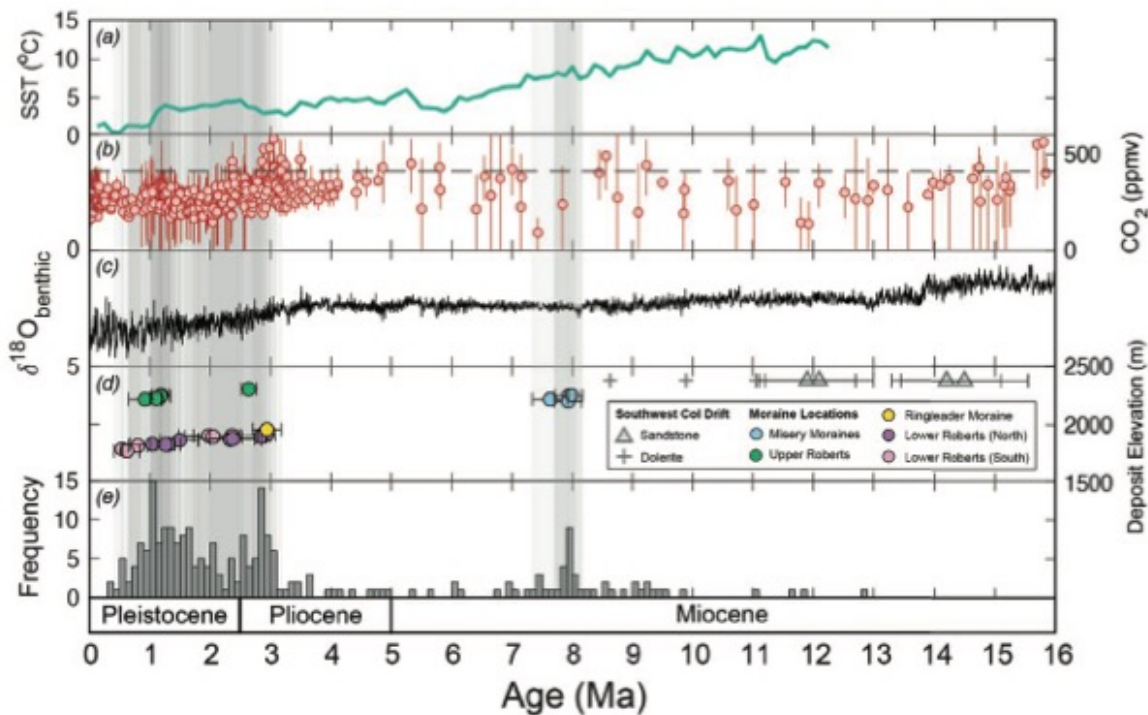
Figure 14: Comparison between Roberts Massif glacial chronology and relevant climate records. (a) Southern Hemisphere alkenone-derived temperature stack (Herbert et al., 2016); (b) Boron-isotope-, paleosol-, and stomata-derived CO_2 records (Beerling et al., 2009; Breecker and Retallack, 2014; Da et al., 2019; Dyez et al., 2018; Ji et al., 2018; Sosdian et al., 2018; Wang et al., 2015; Zhang et al., 2013) (c) benthic oxygen isotope stack (De Vleeschouwer et al., 2017), (d) Moraine age and uncertainty at Roberts Massif, plotted against deposit elevation. Note that deposition of the Misery moraines required ice to be > 300 m thicker than today, which is not reflected in the moraine elevation. The age of the Southwest Col sandstones account for erosion, as described in section 3.2.2 (e) Histogram of all apparent exposure ages at Roberts Massif, including outliers. Vertical gray bars denote moraine ages, including uncertainty. Darker gray color shows a higher frequency of moraines.

Data Availability

689   All analytical information associated with cosmogenic-nuclide measurements appear in the supplementary tables.

690   Analytical information, with additional sample documentation and photographs, is also available in the ICE-

691   D:ANTARCTICA online database (http://antarctica.ice-d.org/).

692 **Author Contribution**

693 All authors conducted fieldwork, sample collection, and sample preparation for cosmogenic-nuclide analyses. Balco,
694 Balter and Thomas carried out cosmogenic noble gas measurements, and were responsible for data reduction and
695 analysis. Balter prepared the manuscript with contributions from Balco and Bromley.

696 **Competing Interests**

697 The authors declare that they have no conflict of interest.

698 **Acknowledgements**

699 This work was supported by U.S. National Science Foundation grants ANT-1443329 and ANT-1443321 and by the
700 Ann and Gordon Getty Foundation. It would not have been possible without major contributions from many elements
701 of the U.S. Antarctic Program, including the 109th Airlift Wing of the New York Air National Guard, pilots and
702 ground crews of Kenn Borek Air, and many USAP staff at Shackleton Glacier Camp and McMurdo Station. In
703 addition, we thank Chris Simmons for field mountaineering support, Tim Becker for assistance with noble gas
704 measurements at BGC, Kaj Overturf for help with sample crushing and sieving at the University of Maine, and Brenda
705 Hall for insightful discussions. Geospatial support for this work was provided by the Polar Geospatial Center under
706 NSF-OPP awards 1043681 and 1559691.

707 **References**

708 Ackert, R. P.: Antarctic glacial chronology : new constraints from surface exposure dating., Ph.D. thesis, Woods
709   Hole Oceanographic Institution, Massachusetts Institute of Technology, United States of America, 213 pp.,
710   2000.

711 Ackert, R. P. and Kurz, M. D.: Age and uplift rates of Sirius Group sediments in the Dominion Range, Antarctica,
712   from surface exposure dating and geomorphology, Glob. Planet. Change, 42, 207–225, 2004.

713 Atkins, C. B.: Geomorphological evidence of cold-based glacier activity in South Victoria Land, Antarctica, Geol.
714   Soc. London, Spec. Publ., 381(1), 299–318, doi:10.1144/SP381.18, 2013.

715 Atkins, C. B., Barrett, P. J. and Hicock, S. R.: Cold glaciers erode and deposit: Evidence from Allan Hills,
716   Antarctica, Geology, 30(7), 659–662, doi:10.1130/0091-7613(2002)030<0659:CGEADE>2.0.CO;2, 2002.

717 Austermann, J., Pollard, D., Mitrovica, J. X., Moucha, R., Forte, A. M., DeConto, R. M., Rowley, D. B. and Raymo,
718   M. E.: The impact of dynamic topography change on Antarctic ice sheet stability during the mid-Pliocene
719   warm period, Geology, 43(10), 927–930, doi:10.1130/G36988.1, 2015.

Bader, N.A., Licht, K.J., Kaplan, M.R., Kassab, C.: East Antarctic ice sheet stability recorded in a high-elevation ice-cored moraine, Quat. Sci. Rev., 159, 88–102, doi: https://doi.org/10.1016/j.quascirev.2016.12.005, 2017.

Balco, G.: The absence of evidence of absence of the East Antarctic Ice Sheet, Geology, 43(10), 943–944, doi:10.1130/focus102015.1, 2015.

Balco, G.: Saturated Surfaces in Antarctica: www.cosmognosis.wordpress.com/2016/09/09/saturated-surfaces-in-antarctica/, last access: 15 February 2020, 2016.

Balco, G. and Shuster, D. L.: ^{26}Al-^{10}Be-^{21}Ne burial dating, Earth Planet. Sci. Lett., 286(3–4), 570–575, doi:10.1016/j.epsl.2009.07.025, 2009a.

Balco, G. and Shuster, D. L.: Production rate of cosmogenic 21Ne in quartz estimated from 10Be, 26Al, and 21Ne concentrations in slowly eroding Antarctic bedrock surfaces, Earth Planet. Sci. Lett., 281(1–2), 48–58, doi:10.1016/j.epsl.2009.02.006, 2009b.

Balco, G., Stone, J. O., Lifton, N. A. and Dunai, T. J.: A complete and easily accessible means of calculating surface exposure ages or erosion rates from 10Be and 26Al measurements, Quat. Geochronol., 3, 174–195, doi:10.1016/j.quageo.2007.12.001, 2008.

Balco, G., Blard, P. H., Shuster, D. L. and Stone, J. O. H.: Cosmogenic and nucleogenic 21Ne in quartz in a 28-meter sandstone core from the McMurdo Dry Valleys, Antarctica, Quat. Geochronol., 52, 63–76, 2019.

Beerling, D. J., Fox, A. and Anderson, C. W.: Quantitative uncertainty analyses of ancient atmospheric co2 estimates from fossil leaves, Am. J. Sci., 309, 775–787, doi:10.2475/09.2009.01, 2009.

Blard, P. H. and Farley, K. A.: The influence of radiogenic 4He on cosmogenic 3He determinations in volcanic olivine and pyroxene, Earth Planet. Sci. Lett., 276, 20–29, doi:10.1016/j.epsl.2008.09.003, 2008.

Blard, P. H., Balco, G., Burnard, P. G., Farley, K. A., Fenton, C. R., Friedrich, R., Jull, A. J. T., Niedermann, S., Pik, R., Schaefer, J. M., Scott, E. M., Shuster, D. L., Stuart, F. M., Stute, M., Tibari, B., Winckler, G. and Zimmermann, L.: An inter-laboratory comparison of cosmogenic 3He and radiogenic 4He in the CRONUS-P pyroxene standard, Quat. Geochronol., 26, 11–19, doi:10.1016/j.quageo.2014.08.004, 2015.

Bockheim, J.G., Wilson, S.C., Denton, G.H., Andersen, B.G., Stuiver, M., 1989. Late Quaternary ice-surface fluctuations of Hatherton Glacier, Transantarctic Mountains. Quat. Res., 31, 229-254.

Borchers, B., Marrero, S., Balco, G., Caffee, M., Goehring, B., Lifton, N., Nishiizumi, K., Phillips, F., Schaefer, J. and Stone, J.: Geological calibration of spallation production rates in the CRONUS-Earth project, Quat. Geochronol., 31, 188–198, doi:10.1016/j.quageo.2015.01.009, 2016.

Breecker, D. O. and Retallack, G. J.: Refining the pedogenic carbonate atmospheric CO2 proxy and application to Miocene CO2, Palaeogeogr. Palaeoclimatol. Palaeoecol., 406, 1–8, doi:10.1016/j.palaeo.2014.04.012, 2014.

Bromley, G.R., Hall, B.L., Stone, J.O. and Conway, H., 2012. Late Pleistocene evolution of Scott Glacier, southern Transantarctic Mountains: implications for the Antarctic contribution to deglacial sea level. Quat. Sci. Rev., 50, 1-13.

Bromley, G. R. M., Hall, B. L., Stone, J. O., Conway, H. and Todd, C. E.: Late Cenozoic deposits at Reedy Glacier, Transantarctic Mountains: implications for former thickness of the West Antarctic Ice Sheet, Quat. Sci. Rev., 29(3–4), 384–398, doi:10.1016/j.quascirev.2009.07.001, 2010.

Bromley, G. R. M., Winckler, G., Schaefer, J. M., Kaplan, M. R., Licht, K. J. and Hall, B. L.: Pyroxene separation by HF leaching and its impact on helium surface-exposure dating, Quat. Geochronol., 23, 1–8, doi:10.1016/j.quageo.2014.04.003, 2014.

Brook, E. J., Kurz, M. D., Ackert Jr., R. P., Denton, G. H., Brown, E. T., Raisbeck, G. M. and Yiou, F.: Chronology of Taylor Glacier Advances in Arena Valley, Antarctica, Using in Situ Cosmogenic 3He and 10Be, Quat. Res., 39, 11–23, 1993.

Brook, E. J., Brown, E. T., Kurz, M. D., Ackert, R. P., Raisbeck, G. M. and Yiou, F.: Constraints on Age, Erosion, and Uplift of Neogene Glacial Deposits in the Transantarctic-Mountains Determined From in-Situ Cosmogenic Be-10 and Al-26, Geology, 23(12), 1063–1066, doi:10.1130/0091-7613(1995)0232.3.CO;2, 1995.

Brown, E. T., Edmond, J. M., Raisbeck, G. M., Yiou, F., Kurz, M. D. and Brook, E. J.: Examination of surface exposure ages of Antarctic moraines using in situ produced 10Be and 26Al, Geochim. Cosmochim. Acta, 55, 2269–2283, doi:10.1016/0016-7037(91)90103-C, 1991.

Bruno, A. L., Baur, H., Graf, T., Schlkhter, C., Signer, P. and Wieler, R.: Dating of Sirius Group tillites in the Antarctic Dry Valleys with cosmogenic 3He and 21Ne, Earth Planet. Sci. Lett., 147, 37–54, doi:http://dx.doi.org/10.1016/S0012-821X(97)00003-4, 1997.

Burke, K. D., Williams, J. W., Chandler, M. A., Haywood, A. M., Lunt, D. J. and Otto-Bliesner, B. L.: Pliocene and Eocene provide best analogs for near-future climates, Proc. Natl. Acad. Sci. U. S. A., 115(52), 13288–13293, doi:10.1073/pnas.1809600115, 2018.

Burnard, P. G. and Farley, K. A.: Calibration of pressure-dependent sensitivity and discrimination in Nier-type noble gas ion sources, Geochemistry, Geophys. Geosystems, 1, doi:10.1029/2000GC000038, 2000.

Da, J., Zhang, Y. G., Li, G., Meng, X. and Ji, J.: Low CO2 levels of the entire Pleistocene epoch, Nat. Commun., 10, 1–9, doi:10.1038/s41467-019-12357-5, 2019.

Denton, G.H., Bockheim, J.G., Wilson, S.C., Leide, J.E., 1989. Late Quaternary ice surface fluctuations of Beardmore Glacier, Transantarctic Mountains. Quat. Res.31, 183-209.

Denton, G.H., Hall, B.L., 2000. Glacial and Paleoclimatic history of the Ross Ice drainage system of Antarctica. Geogr. Ann., 87 A(1), 139-432.

786   Denton, G. H. and Sugden, D. E.: Meltwater features that suggest Miocene ice-sheet overriding of the Transantarctic

787   Mountains in Victoria Land, Antarctica, Geogr. Ann., 87 A(1), 67–85, 2005.

788   Denton, G. H., Sugden, D. E., Marchant, D. R., Hall, B. L. and Thomas, I.: East Antarctic Ice Sheet Sensitivity To

789   Pliocene Climatic Change From a Dry Valleys Perspective, Geogr. Ann., 75(4), 155–204, 1993.

790   Dyez, K. A., Hönisch, B. and Schmidt, G. A.: Early Pleistocene Obliquity-Scale pCO2 Variability at ~1.5 Million

791   Years Ago, Paleoceanogr. Paleoclimatology, 33(11), 1270–1291, doi:10.1029/2018PA003349, 2018.

792   Fitzgerald, P. G.: Thermochronologic constraints on post-Paleozoic tectonic evolution of the central Transantarctic

793   Mountains, Antarctica, Tectonics, 13(4), 818–836, doi:10.1029/94TC00595, 1994.

794   Gasson, E., DeConto, R. M., Pollard, D. and Levy, R. H.: Dynamic Antarctic ice sheet during the early to mid-

795   Miocene, Proc. Natl. Acad. Sci. U. S. A., 113(13), 3459–3464, doi:10.1073/pnas.1516130113, 2016.

796   Gillespie, A. R. and Bierman, P. R.: Precision of terrestrial exposure ages and erosion rates estimated from analysis

797   of cosmogenic isotopes produced in situ, J. Geophys. Res., 100(B12), doi:10.1029/95jb02911, 1995.

798   Goehring, B. M., Muzikar, P. and Lifton, N. A.: Establishing a Bayesian approach to determining cosmogenic

799   nuclide reference production rates using He-3, Earth Planet. Sci. Lett., 481, 91–100,

800   doi:10.1016/j.epsl.2017.10.025, 2018.

801   Golledge, N. R., Marsh, O. J., Rack, W., Braaten, D. and Jones, R. S.: Basal conditions of two Transantarctic

802   Mountains outlet glaciers from observation-constrained diagnostic modelling, J. Glaciol., 60(223), 855–

803   866, doi:10.3189/2014JoG13J131, 2014.

804   Graly, J.A., Licht, K.J., Kassab, C.M., Bird, B.W., Kaplan, M.R.: Warm-based basal sediment entrainment and far-

805   field Pleistocene origin evidenced in central Transantarctic blue ice through stable isotopes and internal

806   structures, J. Glaciol, 64(244), 185-196, doi: 10.1017/jog.2018.4, 2018.

807   Herbert, T. D., Lawrence, K. T., Tzanova, A., Peterson, L. C., Caballero-Gill, R. and Kelly, C. S.: Late Miocene

808   global cooling and the rise of modern ecosystems, Nat. Geosci., 9(11), 843–847, doi:10.1038/ngeo2813,

809   2016.

810   Holbourn, A., Kuhnt, W., Clemens, S., Prell, W. and Andersen, N.: Middle to late Miocene stepwise climate

811   cooling: Evidence from a high-resolution deep water isotope curve spanning 8 million years,

812   Paleoceanography, 28(4), 688–699, doi:10.1002/2013PA002538, 2013.

813   Huybrechts, P.: Glaciological Modelling of the Late Cenezoic East Antarctic Ice Sheet: Stability or Dynamism,

814   Geogr. Ann., 75 A, 221–238, 1993.

815   Ivy-Ochs, S., Schluchter, C., Kubik, P. W., Dittrich-Hannen, B. and Beer, J.: Minimum 10Be exposure ages of early

816   Pliocene for the Table Mountain plateau and the Sirius Group at Mount Fleming, Dry Valleys, Antarctica,

817   Geology, 23(11), 1007–1010, doi:10.1130/0091-7613(1995)023<1007:MBEAOE>2.3.CO;2, 1995.

818 Ji, S., Nie, J., Lechler, A., Huntington, K. W., Heitmann, E. O. and Breecker, D. O.: A symmetrical CO_2 peak and
819   asymmetrical climate change during the middle Miocene, Earth Planet. Sci. Lett., 499, 134–144,
820   doi:10.1016/j.epsl.2018.07.011, 2018.

821 Jull, A. J. T., Scott, E. M. and Bierman, P.: The CRONUS-Earth inter-comparison for cosmogenic isotope analysis,
822   Quat. Geochronol., 26, 3–10, doi:10.1016/j.quageo.2013.09.003, 2015.

823 Kaplan, M. R., Licht, K. J., Winckler, G., Schaefer, J. M., Bader, N., Mathieson, C., Roberts, M., Kassab, C. M.,
824   Schwartz, R. and Graly, J. A.: Middle to Late Pleistocene stability of the central East Antarctic Ice Sheet at
825   the head of Law Glacier, Geology, 45(11), 963–966, doi:10.1130/G39189.1, 2017.

826 Kober, F., Alfimov, V., Ivy-Ochs, S., Kubik, P. W. and Wieler, R.: The cosmogenic 21Ne production rate in quartz
827   evaluated on a large set of existing 21Ne-10Be data, Earth Planet. Sci. Lett., 302, 163–171,
828   doi:10.1016/j.epsl.2010.12.008, 2011.

829 Lal, D.: Cosmic ray labeling of erosion surfaces: in situ nuclide production rates and erosion models, Earth Planet.
830   Sci. Lett., 104, 424–439, 1991.

831 Lear, C. H., Coxall, H., Foster, G. L., Lunt, D. J., Mawbey, E. M., Rosenthal, Y., Sosdian, S. M., Thomas, E. and
832   Wilson, P. A.: Neogene ice volume and ocean temperatures: Insights from infaunal foraminiferal Mg/Ca
833   paleothermometry, Paleoceanography, 30, 1437–1454, doi:10.1002/2015PA002833.Received, 2015.

834 Levy, R., Harwood, D., Florindo, F., Sangiorgi, F., Tripati, R., von Eynatten, H., Gasson, E., Kuhn, G., Tripati, A.,
835   Deconto, R., Fielding, C., Field, B., Golledge, N., McKay, R., Naish, T., Olney, M., Pollard, D., Schouten,
836   S., Talarico, F., Warny, S., Willmott, V., Acton, G., Panter, K., Paulsen, T., Taviani, M., Askin, R., Atkins,
837   C., Bassett, K., Beu, A., Blackstone, B., Browne, G., Ceregato, A., Cody, R., Cornamusini, G., Corrado, S.,
838   Del Carlo, P., Di Vincenzo, G., Dunbar, G., Falk, C., Frank, T., Giorgetti, G., Grelle, T., Gui, Z.,
839   Handwerger, D., Hannah, M., Harwood, D. M., Hauptvogel, D., Hayden, T., Henrys, S., Hoffmann, S.,
840   Iacoviello, F., Ishman, S., Jarrard, R., Johnson, K., Jovane, L., Judge, S., Kominz, M., Konfirst, M.,
841   Krissek, L., Lacy, L., Maffioli, P., Magens, D., Marcano, M. C., Millan, C., Mohr, B., Montone, P.,
842   Mukasa, S., Niessen, F., Ohneiser, C., Passchier, S., Patterson, M., Pekar, S., Pierdominici, S., Raine, I.,
843   Reed, J., Reichelt, L., Riesselman, C., Rocchi, S., Sagnotti, L., Sandroni, S., Schmitt, D., Speece, M.,
844   Storey, B., Strada, E., Tuzzi, E., Verosub, K., Wilson, G., Wilson, T., Wonik, T. and Zattin, M.: Antarctic
845   ice sheet sensitivity to atmospheric CO_2 variations in the early to mid-Miocene, Proc. Natl. Acad. Sci. U.
846   S. A., 113(13), 3453–3458, doi:10.1073/pnas.1516030113, 2016.

847 Lewis, A. R., Marchant, D. R., Ashworth, A. C., Hedenas, L., Hemming, S. R., Johnson, J. V., Leng, M. J.,
848   Machlus, M. L., Newton, A. E., Raine, J. I., Willenbring, J. K., Williams, M. and Wolfe, A. P.: Mid-
849   Miocene cooling and the extinction of tundra in continental Antarctica, Proc. Natl. Acad. Sci., 105(31),
850   10676–10680, doi:10.1073/pnas.0802501105, 2008.

851   Lifton, N., Sato, T. and Dunai, T. J.: Scaling in situ cosmogenic nuclide production rates using analytical
852   approximations to atmospheric cosmic-ray fluxes, Earth Planet. Sci. Lett., 386, 149–160,
853   doi:10.1016/j.epsl.2013.10.052, 2014.

854   Lisiecki, L. E. and Raymo, M. E.: A Pliocene-Pleistocene stack of 57 globally distributed benthic d18O records,
855   Paleoceanography, 20, 1–17, doi:10.1029/2004PA001071, 2005.

856   Margerison, H. R., Phillips, W. M., Stuart, F. M. and Sugden, D. E.: Cosmogenic 3He concentrations in ancient
857   flood deposits from the Coombs Hills, northern Dry Valleys, East Antarctica: Interpreting exposure ages
858   and erosion rates, Earth Planet. Sci. Lett., 230, 163–175, doi:10.1016/j.epsl.2004.11.007, 2005.

859   Mayewski, P. A.: Glacial geology and late Cenozoic history of the Transantarctic Mountains, Antarctica., Ph.D.
860   Thesis, Institute of Polar Studies, The Ohio State University, United States of America, 1975.

861   Mercer, J.H., 1968. Glacial geology of the Reedy glacier area, Antarctica. Geological Society of America Bulletin
862   79, 471-486.

863   Mercer, J. H.: Some observations on the glacial geology of the Beardmore Glacier area, Antarct. Geol. Geophys.,
864   (427–433), 1972.

865   Middleton, J. L., Ackert, R. P. and Mukhopadhyay, S.: Pothole and channel system formation in the McMurdo Dry
866   Valleys of Antarctica: New insights from cosmogenic nuclides, Earth Planet. Sci. Lett., 355–356, 341–350,
867   doi:10.1016/j.epsl.2012.08.017, 2012.

868   Miller, K. G., Kominz, M. A., Browning, J. V., Wright, J. D., Mountain, G. S., Katz, M. E., Sugarman, P. J.,
869   Cramer, B. S., Christie-Blick, N. and Pekar, S. F.: The phanerozoic record of global sea-level change,
870   Science, 310, 1293–1298, doi:10.1126/science.1116412, 2005.

871   Miller, S. R., Fitzgerald, P. G. and Baldwin, S. L.: Cenozoic range-front faulting and development of the
872   Transantarctic Mountains near Cape Surprise, Antarctica: Thermochronologic and geomorphologic
873   constraints, Tectonics, 29(1), 1–21, doi:10.1029/2009TC002457, 2010.

874   Nishiizumi, K.: Preparation of 26Al AMS standards, Nucl. Instruments Methods Phys. Res. Sect. B Beam Interact.
875   with Mater. Atoms, 223–224, 388–392, doi:10.1016/j.nimb.2004.04.075, 2004.

876   Nishiizumi, K., Imamura, M., Caffee, M. W., Southon, J. R., Finkel, R. C. and McAninch, J.: Absolute calibration of
877   10Be AMS standards, Nucl. Instruments Methods Phys. Res. Sect. B Beam Interact. with Mater. Atoms,
878   258, 403–413, doi:10.1016/j.nimb.2007.01.297, 2007.

879   Orombelli, G., Baroni, C., Denton, G.H., 1990. Late Cenozoic glacial history of the Terra Nova Bay region, northern
880   Victoria Land, Antarctica. Geografica Fisica e Dinamica Quaternaria 13, 139-163.

881   Pagani, M., Liu, Z., Lariviere, J. and Ravelo, A. C.: High Earth-system climate sensitivity determined from Pliocene
882   carbon dioxide concentrations, Nat. Geosci., 3, 27–30, doi:10.1038/ngeo724, 2010.

883 Phillips, F. M., Argento, D. C., Balco, G., Caffee, M. W., Clem, J., Dunai, T. J., Finkel, R., Goehring, B., Gosse, J.
884   C., Hudson, A. M., Jull, A. J. T., Kelly, M. A., Kurz, M., Lal, D., Lifton, N., Marrero, S. M., Nishiizumi,
885   K., Reedy, R. C., Schaefer, J., Stone, J. O. H., Swanson, T. and Zreda, M. G.: Quaternary Geochronology
886   The CRONUS-Earth Project : A synthesis, Quat. Geochronol., 31, 119–154, 2016.

887 Pollard, D. and DeConto, R. M.: Contribution of Antarctica to past and future sea-level rise, Nature, 531, 591–597,
888   doi:10.1038/nature17145, 2016.

889 Pollard, D., DeConto, R. M. and Alley, R. B.: Potential Antarctic Ice Sheet retreat driven by hydrofracturing and ice
890   cliff failure, Earth Planet. Sci. Lett., 412, 112–121, doi:10.1016/j.epsl.2014.12.035, 2015.

891 Prentice, M. L., Denton, G. H., Lowell, T. V, Conway, H. C. and Heusser, L. E.: Pre-late Quaternary glaciation of
892   the Beardmore glacier region, Antarctica, Antarct. J. United States, 21, 95–98, 1986.

893 Railsback, L. B., Gibbard, P. L., Head, M. J., Voarintsoa, N. R. G. and Toucanne, S.: An optimized scheme of
894   lettered marine isotope substages for the last 1.0 million years, and the climatostratigraphic nature of
895   isotope stages and substages, Quat. Sci. Rev., 111, 94–106, doi:10.1016/j.quascirev.2015.01.012, 2015.

896 Rovere, A., Raymo, M. E., Mitrovica, J. X., Hearty, P. J., O'Leary, M. J., Inglis, J. D., Leary, M. J. O. and Inglis, J.
897   D.: The Mid-Pliocene sea-level conundrum: Glacial isostasy, eustasy and dynamic topography, Earth
898   Planet. Sci. Lett., 387, 27–33, doi:10.1016/j.epsl.2013.10.030, 2014.

899 Scambos, T. A., Haran, T. M., Fahnestock, M. A., Painter, T. H. and Bohlander, J.: MODIS-based Mosaic of
900   Antarctica (MOA) data sets: Continent-wide surface morphology and snow grain size, Remote Sens.
901   Environ., 111, 242–257, doi:10.1016/j.rse.2006.12.020, 2007.

902 Schaefer, J. M., Ivy-Ochs, S., Wieler, R., Leya, I., Baur, Denton, G. H. and Schluchter, C.: Cosmogenic noble gas
903   studies in the oldest landscape on Earth: surface exposure age of the Dry Valleys, Antarctica, Earth Planet.
904   Sci. Lett., 167, 215–226, 1999.

905 Schaefer, J. M., Denton, G. H., Kaplan, M., Putnam, A., Finkel, R. C., Barrell, D. J. A., Andersen, B. G., Schwartz,
906   R., Mackintosh, A., Chinn, T. and Schlüchter, C.: High-frequency Holocene glacier fluctuations in New
907   Zealand differ from the northern signature, Science, 324, 622–625, doi:10.1126/science.1169312, 2009.

908 Scherer, R. P., DeConto, R. M., Pollard, D. and Alley, R. B.: Windblown Pliocene diatoms and East Antarctic Ice
909   Sheet retreat, Nat. Commun., 7, 1–9, doi:10.1038/ncomms12957, 2016.

910 Seki, O., Foster, G. L., Schmidt, D. N., Mackensen, A., Kawamura, K. and Pancost, R. D.: Alkenone and boron-
911   based Pliocene pCO2 records, Earth Planet. Sci. Lett., 292, 201–211, doi:10.1016/j.epsl.2010.01.037, 2010.

912 Shevenell, A. E., Kennett, J. P. and Lea, D. W.: Middle Miocene ice sheet dynamics, deep-sea temperatures, and
913   carbon cycling: A Southern Ocean perspective, , doi:10.1029/2007GC001736, 2008.

914 Sosdian, S. M., Greenop, R., Hain, M. P., Foster, G. L., Pearson, P. N. and Lear, C. H.: Constraining the evolution
915   of Neogene ocean carbonate chemistry using the boron isotope pH proxy, Earth Planet. Sci. Lett., 498,
916   362–376, doi:10.1016/j.epsl.2018.06.017, 2018.

917 Spector, P., Stone, J., Cowdery, S. G., Hall, B., Conway, H. and Bromley, G.: Rapid early-Holocene deglaciation in
918   the Ross Sea, Antarctica, Geophys. Res. Lett., 44(15), 7817–7825, doi:10.1002/2017GL074216, 2017.

919 Stern, T.A., ten Brink, U.S.: Flexural Uplift of the Transantarctic Mountains, J. Geophys. Res., 94(B8), 10,315-
920   10,330, 1989.

921 Stern, T. A., Baxter, A. K. and Barrett, P. J.: Isostatic rebound due to glacial erosion within the Transantarctic
922   Mountains, Geology, 33(3), 221–224, doi:10.1130/G21068.1, 2005.

923 Stone, J. O.: Air pressure and cosmogenic isotope production, J. Geophys. Res., 105(B10), 23753–59, 2000.

924 Stone, J. O., Balco, G., Sugden, D. E., Caffee, M. W., Sass, L. C. I., Cowdery, S. G. and Siddoway, C.: Holcene
925   Deglaciation of Marie Byrd Land, West Antarctica, Science, 299(5603), 99–102,
926   doi:10.1126/science.1115233, 2003.

927 Strasky, S., Di Nicola, L., Baroni, C., Salvatore, M. C., Baur, H., Kubik, P. W., Schlüchter, C. and Wieler, R.:
928   Surface exposure ages imply multiple low-amplitude Pleistocene variations in East Antarctic Ice Sheet,
929   Ricker Hills, Victoria Land, Antarct. Sci., 21(1), 59–69, doi:10.1017/S0954102008001478, 2009.

930 Sugden, D. and Denton, G.: Cenozoic landscape evolution of the Convoy Range to Mackay Glacier area,
931   Transantartic Mountains: Onshore to offshore synthesis, Bull. Geol. Soc. Am., 116(7–8), 840–857,
932   doi:10.1130/B25356.1, 2004.

933 Sugden, D. E. ., Marchant, D. R. . and Denton, G. H. .: The Case for a Stable East Antarctic Ice Sheet, Geogr. Ann.
934   Ser. A Phys. Geogr., 75(4), 151–154, 1993.

935 Swanger, K. M., Marchant, D. R., Schaefer, J. M., Winckler, G. and Head, J. W.: Elevated East Antarctic outlet
936   glaciers during warmer-than-present climates in southern Victoria Land, Glob. Planet. Change, 79, 61–72,
937   doi:10.1016/j.gloplacha.2011.07.012, 2011.

938 Todd, C., Stone, J., Conway, H., Hall, B. and Bromley, G.: Late Quaternary evolution of Reedy Glacier, Antarctica,
939   Quat. Sci. Rev., 29(11–12), 1328–1341, doi:10.1016/j.quascirev.2010.02.001, 2010.

940 Vermeesch, P., Balco, G., Blard, P. H., Dunai, T. J., Kober, F., Niedermann, S., Shuster, D. L., Strasky, S., Stuart, F.
941   M., Wieler, R. and Zimmermann, L.: Interlaboratory comparison of cosmogenic21Ne in quartz, Quat.
942   Geochronol., 26(1), 20–28, doi:10.1016/j.quageo.2012.11.009, 2015.

943 De Vleeschouwer, D., Vahlenkamp, M., Crucifix, M. and Pälike, H.: Alternating Southern and Northern
944   Hemisphere climate response to astronomical forcing during the past 35 m.y, Geology, 45(4), 375–378,
945   doi:10.1130/G38663.1, 2017.

946   Wang, Y., Momohara, A., Wang, L., Lebreton-Anberrée, J. and Zhou, Z.: Evolutionary history of atmospheric CO2
947   during the late cenozoic from fossilized metasequoia needles, PLoS One, 10(7), 1–15,
948   doi:10.1371/journal.pone.0130941, 2015.

949   Van der Wateren, F. M., Dunai, T. J., Van Balen, R. T., Klas, W., Verbers, A. L. L. M., Passchier, S. and Herpers,
950   U.: Contrasting neogene denudation histories of different structural regions in the transantarctic mountains
951   rift flank constrained by cosmogenic isotope measurements, Glob. Planet. Change, (23), 145–172, 1999.

952   Webb, P. N., Harwood, D. M., McKelvey, B. C., Mercer, J. H. and Stott, L. D.: Cenozoic marine sedimentation and
953   ice-volume variation on the East Antarctic craton., Geology, 12, 287–291, doi:10.1130/0091-
954   7613(1984)12<287:CMSAIV>2.0.CO;2, 1984.

955   Wilch, T. I., Lux, D. R., Denton, G. H. and McIntosh, W. C.: Minimal Pliocene-Pleistocene uplift of the dry valleys
956   sector of the Transantarctic Mountains: a key parameter in ice-sheet reconstructions, Geology, 21(9), 841–
957   844, doi:10.1130/0091-7613(1993)021<0841:MPPUOT>2.3.CO;2, 1993.

958   Willeit, M., Ganopolski, A., Calov, R. and Brovkin, V.: Mid-Pleistocene transition in glacial cycles explained by
959   declining CO2 and regolith removal, Sci. Adv., 5(4), 1–8, doi:10.1126/sciadv.aav7337, 2019.

960   Winnick, M. J. and Caves, J. K.: Oxygen isotope mass-balance constraints on Pliocene sea level and East Antarctic
961   Ice Sheet stability, Geology, 43(10), 879–882, doi:10.1130/G36999.1, 2015.

962   Zhang, Y. G. Y. G., Pagani, M., Liu, Z., Bohaty, S. M. S. M. and DeConto, R.: A 40-million-year history of
963   atmospheric CO2, Philos. Trans. R. Soc. A, 371, 1–20, 2013.

964